Monthly Notices of the ROYAL ASTRONOMICAL SOCIETY

MNRAS **543,** 1816–1832 (2025) https://doi.org/10.1093/mnras/staf1580
Advance Access publication 2025 September 17

Dynamical measurement of supermassive black hole masses: QPE timing method

Cong Zhou [1,2] Zhen Pan,[3,4]★ Ning Jiang [1,2]★ and Wen Zhao[1,2]★

[1]*Department of Astronomy, University of Science and Technology of China, Hefei 230026, P. R. China*
[2]*School of Astronomy and Space Sciences, University of Science and Technology of China, Hefei 230026, P. R. China*
[3]*Tsung-Dao Lee Institute, Shanghai Jiao-Tong University, 520 Shengrong Road, Shanghai 201210, P. R. China*
[4]*School of Physics & Astronomy, Shanghai Jiao-Tong University, 800 Dongchuan Road, Shanghai 200240, P. R. China*

Accepted 2025 September 15. Received 2025 September 15; in original form 2025 May 9

ABSTRACT

Quasi-periodic eruptions (QPEs) are intense repeating soft X-ray bursts with recurrence times about a few hours to a few weeks from galactic nuclei. More and more analyses show that (at least a fraction of) QPEs are the result of collisions between a stellar mass object (SMO, a stellar mass black hole or a main-sequence star) and an accretion disc around a supermassive black hole (SMBH) in galactic nuclei. Previous studies have shown the possibility of reconstructing the SMO trajectory from QPE timing data, consequently measuring the SMBH mass from tracing a single SMO. In this paper, we construct a comprehensive Bayesian framework for implementing the QPE timing method, explore the optimal QPE observation strategy for measuring SMBH masses, and forecast the measurement precision expected in the era of multitarget X-ray telescope, Chasing All Transients Constellation Hunters (CATCH). Simulations of CATCH observations of GSN 069 and eRO-QPE2 like QPEs confirm the possible applications of the QPE timing method in precise measurement of SMBH masses (and spins), especially in the lower mass end ($\lesssim 10^7\,\mathrm{M}_\odot$) where QPEs prevail and relevant dynamical time-scales are reasonably short to be measured.

Key words: black hole physics – galaxies: active – quasars: supermassive black holes – transients: tidal disruption events.

1 INTRODUCTION

It is nowadays widely accepted that supermassive black holes (SMBHs) with masses ranging from $\sim 10^5 - 10^{10}\ \mathrm{M}_\odot$ reside at the centres of most, if not all, massive galaxies with substantial spheroidal (bulge) components, both quiescent and active (see reviews by Kormendy & Richstone 1995; Kormendy & Ho 2013). However, a precise measurement of the the masses of SMBHs ($M_\bullet$) has been a challenge since it is of great difficulty to directly probe the motion of objects in the vicinity of SMBHs, where the gravitational potential of the SMBHs exerts a dominant influence. In fact, aside from Sagittarius A* at the centre of our Milky Way (Schödel et al. 2002; Ghez et al. 2005; Gillessen et al. 2009; GRAVITY Collaboration 2018), we have not been able to effectively resolve individual stars or gas clouds around SMBHs. Instead, we can only measure the collective motion of stars or gas within a given region as a whole even taking advantage of highly spatially resolved observations of *Hubble Space Telescope* and large adaptive optics-assisted ground-based telescopes. Therefore, the $M_\bullet$ measurement suffers from additional uncertainties from velocity smoothing and galaxy central mass distribution in the dynamical modelling. So far, only a total of hundreds of SMBHs in the local galaxies ($\lesssim 100$ Mpc) have been weighted by the so-called stellar and gas kinematics. Moreover, these SMBHs are found to be correlated with the bulge properties of their host galaxies, most commonly known as the $M_\bullet$–$\sigma_\star$ relation in which the $\sigma_\star$ refers to the stellar velocity dispersion (Ferrarese & Merritt 2000; Gebhardt et al. 2000), making the field of BH–galaxy co-evolution a frontier of astronomy over the past two decades (see reviews by Kormendy & Ho 2013; Heckman & Best 2014). These correlations themselves offer a new and more convenient approach to estimate the $M_\bullet$ since the kinematic method used in local massive galaxies cannot be extended to more distant or dwarf galaxies.

Although the $M_\bullet - \sigma_\star$ and the $M_\bullet - M_\star$ relations have been widely used to infer $M_\bullet$ when the host bulge mass $M_\star$ or the stellar velocity dispersion $\sigma_\star$ is available, it is important to recognize their uncertainties, i.e. $0.3 - 0.4$ dex intrinsic scatter even when only considering elliptical galaxies and classical bulges (Gültekin et al. 2009; Kormendy & Ho 2013; McConnell & Ma 2013). Furthermore, these relations are primarily established based on SMBHs with $M_\bullet \gtrsim 10^7\ \mathrm{M}_\odot$, leading to larger uncertainties for lower mass black holes, i.e. $M_\bullet \lesssim 10^6\ \mathrm{M}_\odot$, either due to a larger intrinsic scatter or a possible systematic error.

For active galactic nuclei (AGNs), perhaps the most popular method of measuring $M_\bullet$ is the virial mass, which assumes that the broad-line region (BLR) is virialized and the motions of clouds are governed by the gravity of SMBH (see reviews by Shen 2013; Peterson 2014). There is a vague coefficient f in the calculation whose average value is calibrated by the $M_\bullet$–$\sigma_\star$ relation. It means, in principle, that the virial mass estimator can not be more accurate

★ E-mail: zhpan@sjtu.edu.cn (ZP), jnac@ustc.edu.cn (NJ), wzhao7@ustc.edu.cn (WZ)

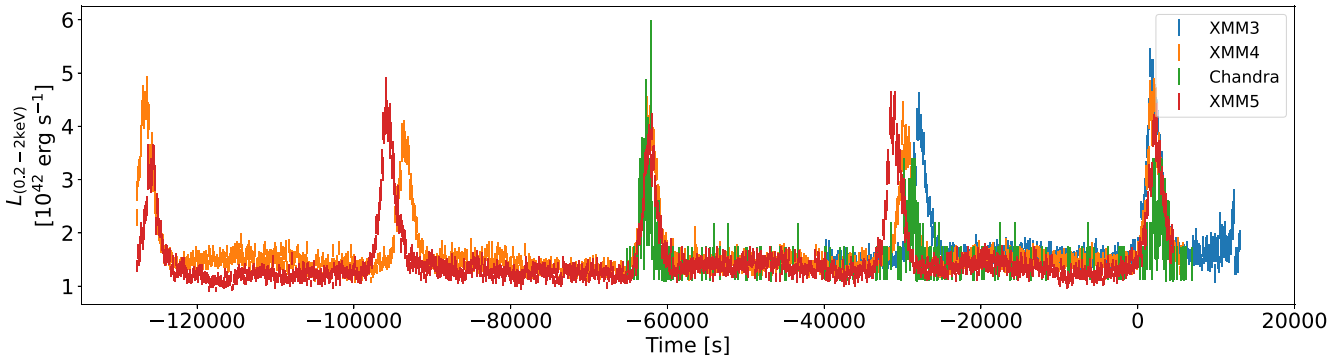

Figure 1. GSN 069 QPE light curves from four observations during 2018 December–2019 May (Miniutti et al. 2019, 2023a), where the recurrence times show an alternating long-short pattern $T_{\mathrm{long,short}}$, with both T_{long} and T_{short} showing clear variations, while the sum of two consecutive recurrence times $T_{\mathrm{long}} + T_{\mathrm{short}}$ remains approximately a constant (Zhou et al. 2024a).

than $M_\bullet$–$\sigma_\star$ relation. Moreover, f is likely to vary from object to object, since it depends on the kinematics, geometry, inclination of the clouds, and even the types of the bulges (Ho & Kim 2014). Recently, the evolutionary NIR interferometry GRAVITY, mounted on the Very Large Telescope Interferometer, has opened up a new era of probing the BLR structure and has great potential to improve the precision of the $M_\bullet$ measurement (Gravity Collaboration 2018; Abuter et al. 2024), but it can only apply to very few K-band luminous AGNs. In addition, many other observational properties of AGNs, i.e. X-ray variability amplitude (McHardy et al. 2006; Ponti et al. 2012; Pan et al. 2015) and optical variability time-scale (Burke et al. 2021), have been suggested to correlate with $M_\bullet$, though their underlying physics and uncertainties remain poorly understood.

In this paper, we propose a novel method to measure the $M_\bullet$ with unprecedented precision using the quasi-periodic eruption (QPE) phenomenon. QPEs are intense repeating soft X-ray bursts with recurrence times about a few hours to a few weeks from galactic nuclei nearby. Starting from the first detection more than a decade ago (Sun, Shu & Wang 2013), QPEs from about 10 different nearby galactic nuclei have been reported (Miniutti et al. 2019; Giustini, Miniutti & Saxton 2020; Arcodia et al. 2021; Chakraborty et al. 2021; Arcodia et al. 2022, 2024a; Evans et al. 2023; Guolo et al. 2024; Nicholl et al. 2024; Chakraborty et al. 2025; Hernández-García et al. 2025). The QPEs are detected in the soft X-ray band with similar peak luminosities ($10^{42} - 10^{43}$ erg s^{-1}), thermal-like X-ray spectra with temperature $kT \simeq 100 - 250$ eV and the temperature $50 - 80$ eV in the quiescent state.

Though there have been some debates on the origin of QPEs, more and more analyses favor the extreme mass ratio inspiral (EMRI) + accretion disc model, where the QPEs are the result of collisions between a stellar mass object (SMO, a stellar mass black hole or a main-sequence star) and an accretion disc around an SMBH in galactic nuclei (see e.g. Xian et al. 2021; Franchini et al. 2023; Tagawa & Haiman 2023; Linial & Metzger 2023, 2024b; Chakraborty et al. 2024; Giustini et al. 2024; Guolo et al. 2024; Linial & Metzger 2024a; Linial & Quataert 2024; Arcodia et al. 2024a, c; Pasham et al. 2024a; Zhou et al. 2024a, 2024b; Pasham et al. 2024b; Miniutti et al. 2025; Vurm, Linial & Metzger 2025; Yao et al. 2025; Zhou, Zeng & Pan 2025 for details). Among all the observations, two pieces of direct observational evidence for the EMRI + disc model have been recognized. Recently, QPEs in X-ray light curves of three tidal disruption events (TDEs) $\mathcal{O}(1)$ years after their ignitions have been directly detected (Nicholl et al. 2024; Bykov et al. 2025; Chakraborty et al. 2025). Moreover, the QPE and TDE hosts show strikingly morphological similarities (Gilbert et al. 2024) and a preference for extending emission-line regions indicative of recently faded AGNs (Wevers et al. 2024). The other observational evidence is about the alternating long-short pattern in the QPE recurrence times which has long been noticed in several QPE sources (Miniutti et al. 2019; Giustini et al. 2020; Arcodia et al. 2021, 2022), including the most famous source GSN 069. A more intriguing feature in the QPE timing was identified by Zhou et al. (2024a): there are large variations in both the long and the short recurrence times of GSN 069 QPEs $T_{\mathrm{long,short}}(t)$, while $T_{\mathrm{long}}(t) + T_{\mathrm{short}}(t)$ remains nearly a constant (see Fig. 1). This observation strongly implies that $T_{\mathrm{long}} + T_{\mathrm{short}}$ is the fundamental period of underlying physical process that is sourcing the QPEs, and two flares with varying intervals are produced per fundamental period. These two observations naturally fit in the EMRI + disc model (see Fig. 2), while are hardly explained by other models in a natural way. Therefore, a unified model proposes that both TDEs and QPEs are the embers of AGNs, where AGNs increase both the TDE rate and the formation rate of low eccentricity EMRIs, and QPEs are preferentially found in recently faded AGNs, where TDEs often feed a misaligned accretion disc to the EMRI (Jiang & Pan 2025).

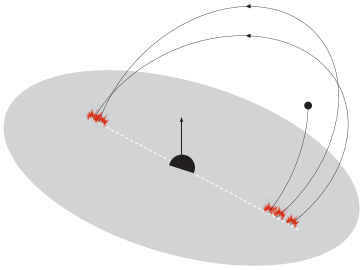

Figure 2. Schematic picture of the EMRI + disc model, where the EMRI collides the disc at a different location each time due to apsidal precession, and the EMRI orbital plane precesses on an even longer Lense–Thirring precession time-scale if the central SMBH is spinning.

In the framework of EMRI + disc model, a range of astrophysical applications of QPEs have been investigated, including measuring SMBH parameters, probing structure of SMBH accretion discs, formation processes, and formation rates of EMRIs (Xian et al. 2021; Kaur, Rom & Sari 2025; Zhou et al. 2024a, b, 2025; Arcodia et al. 2024b) and implications for potential multimessenger observations

of EMRIs in the era of spaceborne gravitational wave astrophysics (Kejriwal et al. 2024). In this work, we will focus on measuring SMBH masses with QPE timing data, which we have briefly discussed in previous works (Zhou et al. 2024a, b, 2025; hereafter Papers I–III). Using the QPE timing method, one can reconstruct the trajectory of a single SMO around an SMBH, therefore accurately measure the orbital parameters and the SMBH mass.

The QPE timing method is a truly direct dynamic measurement achieved by tracing the motion of a single star orbiting around an SMBH, thereby circumventing many uncertainties related to both measurement and systematic errors involved in traditional methods. This method is in the same spirit of measuring the Sagittarius A* SMBH mass by monitoring orbits of individual stars (Schödel et al. 2002; Ghez et al. 2005; Gillessen et al. 2009; GRAVITY Collaboration 2018). As QPEs are preferred to be found in dwarf galaxies hosting low-mass black holes (Wevers et al. 2022), this technique is particularly valuable as all previous methods are much less accurate in the low-mass range (Greene, Strader & Ho 2020). For example, the mass $M_\bullet$ of the prototype and most well-studied intermediate-mass black hole (IMBH) in the nearby AGN NGC 4395 has a huge mass uncertainty between 4×10^5 and 1×10^4 $M_\odot$ reported by various works (Peterson et al. 2005; den Brok et al. 2015; Woo et al. 2019). In this regard, the QPE timing method we proposed will also aid in the detection of IMBHs with robust mass measurement, particularly in inactive galaxies throughout the universe.

Existing light-curve data of QPEs have been obtained using *XMM–Newton* (Miniutti et al. 2019, 2023a, b; Arcodia et al. 2021, 2024c), *Chandra* (Miniutti et al. 2023a), and NICER (Arcodia et al. 2021; Chakraborty et al. 2024; Nicholl et al. 2024). Among these instruments, *XMM–Newton* provides the highest quality data but its observation epochs typically span only about one day. The precision of mass measurement is expected to improve substantially with extended-duration monitoring.

The Chasing All Transients Constellation Hunters (CATCH; Li et al. 2023), proposed by the Institute of High Energy Physics at the Chinese Academy of Sciences, comprises a constellation of ~ 100 satellites aiming to conduct simultaneous follow-up observations for diverse transients in the X-ray band. On 2024 June 22, the first CATCH pathfinder (Huang et al. 2024) was launched alongside the Space-based multiband astronomical Variable Objects Monitor mission (Götz et al. 2009). The complete constellation is projected to be deployed in the early 2030s. CATCH uses the WALKER constellation design with three orbital planes, each of which consists of a few tens of satellites. This configuration enables uninterrupted (long-term) monitoring mode (Li et al. 2023), effectively allowing continuous observation of a source. A small number of satellites can be fully reserved for QPE observations.[1] In this paper, we forecast the potential contribution of CATCH to the $M_\bullet$ measurement and compare its capabilities with those of current instruments.

This paper is organized as follows. In Section 2, we illustrate the underlying principles of the QPE timing method. In Section 3, we introduce the details of the Bayesian framework for QPE timing analysis. In Section 4, we simulate four strategies to demonstrate the capability of measuring $M_\bullet$ of QPE timing method and two more strategies to demonstrate the unique potential of CATCH to measure a. Summary and discussions are given in Section 5.

[1]Private communication with Lian Tao, PI of CATCH.

Throughout this paper, we will use geometric units with convention $G = c = 1$.

2 BASIC PRINCIPLES OF THE QPE TIMING METHOD

The physical picture of constraining the SMBH mass from QPE timing is rather simple. As the SMO orbiting around the SMBH, it crosses the accretion disc twice and produces two flares per orbit. Therefore, there is an alternating long-short pattern in the QPE recurrence times, arising from the orbital eccentricity and different light path length from the two collision locations to the observer. The orbital period can be identified as $T_{\rm obt} = T_{\rm long} + T_{\rm short}$ to a good precision, where $T_{\rm long}$ and $T_{\rm short}$ are the adjacent QPE recurrence times. Different from in Newtonian gravity, the EMRI orbit in the curved space–time does not close itself due to the apsidal precession. As a result, both $T_{\rm long}$ and $T_{\rm short}$ are time dependent and vary on the time-scale of the apsidal precession period $T_{\rm aps}$. Both periods $T_{\rm obt}$ and $T_{\rm aps}$ can be constrained with a reasonable amount of QPE timing data, and are related to the SMBH mass $M_\bullet$ and the semimajor axis A of the EMRI orbit via the *Kepler*'s third law

$$T_{\rm obt} = 2\pi \left(\frac{A}{M_\bullet}\right)^{3/2} M_\bullet \,, \tag{1}$$

and the ratio

$$\frac{T_{\rm aps}}{T_{\rm obt}} = \frac{p}{3M_\bullet} \approx \frac{A}{3M_\bullet} \,, \tag{2}$$

where p is the semilatus rectum relating to the semimajor axis A and the orbital eccentricity e as $A = p/(1-e^2)$, the approximation sign in the equation above is accurate for low-eccentricity orbits. With the two observables $T_{\rm obt}$ and $T_{\rm aps}$, one can naturally constrain the SMBH mass with $M_\bullet \propto T_{\rm obt}^{5/2} T_{\rm aps}^{-3/2}$.

Note that the two periods measured in the observer frame are different from their intrinsic values by a factor of $(1+z)$ due to the cosmology redshift z, therefore the SMBH mass $M_\bullet$ derived above is in fact a redshifted mass, which is different from the intrinsic mass by a factor of $(1+z)$. The differences are small for currently detected QPE sources at low redshifts $z \sim \mathcal{O}(0.01)$, but could be important for sources at high redshifts.

In a similar way, one can constrain the Lense–Thirring precession period $T_{\rm LT}$ of the EMRI orbit from the QPE timing data if the QPE source has been monitored for a sufficiently long time $\gtrsim T_{\rm LT}$. Consequently, one can infer the dimensionless spin a of the SMBH via the relation

$$\frac{T_{\rm LT}}{T_{\rm obt}} = \frac{1}{2a}\left(\frac{p}{M_\bullet}\right)^{3/2} . \tag{3}$$

In practice, we choose to conduct the QPE timing analysis in the Bayesian framework, the basic ingredients of which have been shown in previous works (Papers I–III). In this work, we aim to generalize the previous analyses and construct a QPE timing method which is capable of measuring orbital parameters and SMBH masses $M_\bullet$ (and spins a) in a comprehensive Bayesian framework.

To summarize, both the SMBH mass and spin can be obtained from the three periods $T_{\rm obt}$, $T_{\rm aps}$, $T_{\rm LT}$ via equations (1)–(3), which are intrinsic properties of Kerr geodesics and are independent of the existence of an accretion disc or not. In the following section, we will explain the details of how to measure these three periods along with disc motion parameters from QPE observations of an EMRI + disc system, where the disc could either be an equatorial disc or a misaligned and precessing disc.

3 BAYESIAN FRAMEWORK FOR QPE TIMING ANALYSIS

As discussed in previous studies, one can predict the SMO-disc collision times and the resulting QPE light curve with a model of SMO motion and an accretion disc model. But the full light prediction is subject to large uncertainties in the disc model, the nature of the SMO, and the radiation mechanism. We therefore choose to constrain the EMRI kinematics and the QPE emission separately for mitigating the impact of these uncertainties. We first fit each QPE with a simple light-curve model and obtain the starting time of each flare $t_0 \pm \sigma(t_0)$ (see Papers I–III for details), which is identified as the time of the SMO crossing the disc and is used for constraining the SMO orbital parameters. With data $d = \{t_0^{(k)} \pm \sigma^{(k)}(t_0)\}$ (k is the flare index) and a QPE flare timing model, we can constrain model parameters Θ in the Bayesian inference framework. According to the Bayes theorem, the posterior of model parameters is written as

$$\mathcal{P}(\Theta, \mathcal{H}|d) = \frac{\mathcal{L}(d|\Theta, \mathcal{H})\pi(\Theta, \mathcal{H})}{\mathcal{Z}(d)} , \tag{4}$$

where $\mathcal{L}(d|\Theta, \mathcal{H})$ is the likelihood of detecting data d under hypothesis $\mathcal{H}$ with model parameters Θ, $\pi(\Theta, \mathcal{H})$ is the assumed prior for model parameters Θ in $\mathcal{H}$, and the normalization factor $\mathcal{Z}(d)$ is the evidence of hypothesis $\mathcal{H}$ with data d.

To quantify the support for one hypothesis $\mathcal{H}_1$ over another $\mathcal{H}_0$ by data d, we can calculate the evidence ratio of two hypotheses, i.e. the Bayes factor,

$$\mathcal{B}_0^1 = \frac{\mathcal{Z}_1(d)}{\mathcal{Z}_0(d)} . \tag{5}$$

The larger $\mathcal{B}_0^1$ represents stronger support for hypothesis $\mathcal{H}_1$ over $\mathcal{H}_0$. In Jeffreys' scale, $\log \mathcal{B}_0^1 \in (1.2, 2.3), (2.3, 3.5), (3.5, 4.6), (4.6, \infty)$ are the criteria of substantial, strong, very strong, and decisive strength of evidence, respectively.

In the following subsections, we will explain the two major components of the QPE timing model (EMRI trajectories and disc motion), define the likelihood for the Bayesian framework of the QPE timing method for measuring SMBH masses.

3.1 Forced EMRI trajectories

As shown in Paper III, the SMO orbital energy dissipation as crossing the accretion disc is small but can be measured in some QPE sources via long-term monitoring. In this subsection, we briefly review the steps of computing forced EMRI trajectories in the Kerr space–time. We start from time-like geodesics in the Kerr space–time, analytic solutions to which have been derived by Fujita & Hikida (2009) and van de Meent (2020) as

$$\begin{aligned}
r(\lambda) &= r(q_r(\lambda); E, L, C) , & q_r(\lambda) &= \Upsilon_r \lambda + q_{r,\rm ini} , \\
z(\lambda) &= z(q_z(\lambda); E, L, C) , & q_z(\lambda) &= \Upsilon_z \lambda + q_{z,\rm ini} , \\
t(\lambda) &= t(q_{t,r,z}(\lambda); E, L, C) , & q_t(\lambda) &= \Upsilon_t \lambda + q_{t,\rm ini} , \\
\phi(\lambda) &= \phi(q_{\phi,r,z}(\lambda); E, L, C) , & q_\phi(\lambda) &= \Upsilon_\phi \lambda + q_{\phi,\rm ini} ,
\end{aligned} \tag{6}$$

where λ is the Mino time; $\{E, L, C\}$ are the energy, angular momentum, and the Carter constant, respectively; $\{\Upsilon_r, \Upsilon_z, \Upsilon_t, \Upsilon_\phi\}$ are the Mino time frequencies in the r, $z(=\cos\theta)$, t, ϕ direction, respectively; and $\{q_{r,\rm ini}, q_{z,\rm ini}, q_{t,\rm ini}, q_{\phi,\rm ini}\}$ are the initial phases. The conversion relation between the constants $\{E, L, C\}$ and the orbital parameters $\{p, e, \cos\theta_{\rm min}\}$ can be found in Schmidt (2002), where $\theta_{\rm min}$ is the minimum polar angle that the geodesic can reach. A geodesic is uniquely determined by a set of orbital parameters $\{p, e, \cos\theta_{\rm min}\}$ and initial phases $\{q_{r,\rm ini}, q_{z,\rm ini}, q_{\phi,\rm ini}\}$ at initial time $t_{\rm ini}$, where the initial phase $q_{t,\rm ini}$ is fixed by $t(q_{t,\rm ini}, q_{r,\rm ini}, q_{z,\rm ini}) = t_{\rm ini}$.

Assuming the orbital energy dissipation as the SMO crosses the accretion disc is a small perturbation, then the SMO trajectories can be formulated as perturbed geodesics with varying constants $\{E(t), L(t), C(t)\}$. In the language of perturbation techniques, the forced EMRI trajectories can be computed using the method of osculating orbits, i.e. in the adiabatic approximation, the equations of motion can be written as

$$\begin{aligned}
r(\lambda) &= r(q_r(\lambda); E, L, C) , & \frac{{\rm d}q_r}{{\rm d}\lambda} &= \Upsilon_r(E, L, C) , \\
z(\lambda) &= z(q_z(\lambda); E, L, C) , & \frac{{\rm d}q_z}{{\rm d}\lambda} &= \Upsilon_z(E, L, C) , \\
t(\lambda) &= t(q_{t,r,z}(\lambda); E, L, C) , & \frac{{\rm d}q_t}{{\rm d}\lambda} &= \Upsilon_z(E, L, C) , \\
\phi(\lambda) &= \phi(q_{\phi,r,z}(\lambda); E, L, C) , & \frac{{\rm d}q_\phi}{{\rm d}\lambda} &= \Upsilon_\phi(E, L, C) ,
\end{aligned} \tag{7}$$

with time-dependent $\{E, L, C\}$ and thereby time-dependent frequencies $\Upsilon_{r,z,t,\phi}$.

The time dependence of $\{E, L, C\}$ can be derived from the change of orbital parameters of $\{T_{\rm obt}(p, e), e, \cos\theta_{\rm min}\}$ as the SMO crosses the disc. As shown in several recent studies of star–disc collisions (e.g. Linial & Metzger 2023; Wang, Zhu & Lin 2024), the relative changes in orbital parameters are similar in magnitudes with $\delta e/e \sim \delta T_{\rm obt}/T_{\rm obt} \sim \delta\theta_{\rm min}/\theta_{\rm min}$. As we have shown in previous studies, $T_{\rm obt}$ is the best-constrained orbital parameter, while e and $\cos\theta_{\rm min}$ are less constrained with $\mathcal{O}(1)$ fractional uncertainties. As a result, the small fractional change in the orbital period $\delta T_{\rm obt}$ is detectable, while δe and $\delta\theta_{\rm min}$ are undetectable for the QPE sources currently available. We therefore can safely take $\dot{e} = \dot{\theta}_{\rm min} = 0$ in calculating the EMRI trajectories. As for the orbital period decay rate $\dot{T}_{\rm obt}(t)$, we model it as

$$\dot{T}_{\rm obt}(t) = \dot{T}_{\rm obt,max} \sin\iota_{\rm sd}(t) , \tag{8}$$

where $\iota_{\rm sd}$ the angle between the SMO orbital plane and the disc plane. This function form is motivated by the energy loss for a star crossing an accretion disc (Linial & Metzger 2023; Linial & Quataert 2024). For a precessing misaligned disc, $\iota_{\rm sd}$ is modulated by the disc precession and the SMO orbital precession, therefore the decay rate $\dot{T}_{\rm obt}$ is non-uniform. In the case of an equatorial accretion disc, the orbital period decay rate simplifies as a constant.

3.2 Disc motion: precession and alignment

In general, a TDE star that is scattered into the tidal radius of an SMBH is from a random direction. As a result, the initial orientation of the accretion disc formed in a TDE is also random. The possible signature of the disc precession on the QPE timing has been discussed in several previous studies (e.g. Franchini et al. 2023; Chakraborty et al. 2024; Arcodia et al. 2024c; Miniutti et al. 2025). As a minimal assumption of the disc precession, we model it as a rigid body-like precession with a constant precession rate. The normal vector of the disck plane is written as

$$\boldsymbol{n}_{\rm disc} = (\sin\beta\cos\alpha, \sin\beta\sin\alpha, \cos\beta) , \tag{9}$$

where $\alpha \in (0, 2\pi)$ is the azimuth angle and $\beta \in (0, \pi/2)$ is the angle between the disc plane and the equatorial plane. With the constant precession rate assumption, the azimuth angle then evolves as

$$\alpha(t) = \alpha_{\rm ini} + \frac{2\pi}{\tau_{\rm p}}(t - t_{\rm ini}) , \tag{10}$$

where $\tau_{\rm p}$ is the disc precession period, and $\alpha_{\rm ini}$ is the initial value of the azimuth angle at $t_{\rm ini}$.

In the long run, the initially misaligned disc is expected to approach the equator plane gradually. One can in principle constrain the evolution history of the inclination angle $\beta(t)$ in a non-parametric approach if sufficiently dense observations of QPEs are available. However, QPE sources are usually sparsely monitored due to limited X-ray observation resources. In practice, we choose to bridge the spare observations with a simple function

$$\sin\beta(t) = \sin\beta_{\rm ini}\exp\left\{-\frac{t-t_{\rm ini}}{\tau_{\rm a}}\right\}\ , \tag{11}$$

parametrizing the alignment process with the alignment time-scale parameter $\tau_{\rm a}$, where $\beta_{\rm ini}$ in the initial value of the disc inclination angle. This function form is motivated by the eigen-mode analysis of disc alignment process (e.g. Scheuer & Feiler 1996; Zanazzi & Lai 2019).

3.3 QPE timing model

In the previous two subsections, we have summarized the key points in modelling the EMRI motion and the disc motion, based on which one can construct a full QPE timing model. But not all the ingredients are necessary for modelling each QPE source, e.g. no evidence for disc precession in GSN 069 QPEs is found (Zhou et al. 2025). Therefore, we consider the following two hypotheses with slightly different assumptions about the EMRI and the disc motion, and the data favoured hypothesis will be selected by Bayesian analyses:

(i) *Vanilla hypothesis ($\mathcal{H}_0$).* The SMO moves around the SMBH losing orbital energy as crossing the equatorial accretion disc. The EMRI + disc system can be specified by nine parameters: the intrinsic orbital parameters $(p, e, \theta_{\rm min})$, the initial phases $(q_{r,\rm ini}, q_{z,\rm ini}, q_{\phi,\rm ini})$, the mass of the SMBH $M_\bullet$ or equivalently the orbital period $T_{\rm obt}$ (equation 1), the dimensionless spin of the SMBH a and the orbital period decay rate $\dot{T}_{\rm obt}$.

(ii) *D isc precession and alignment hypothesis ($\mathcal{H}_1$).* Different from the vanilla hypothesis, we consider a misaligned disc with initial orientation angles $(\alpha_{\rm ini}, \beta_{\rm ini})$ and precessing around the polar direction with a constant period $\tau_{\rm p}$. In this hypothesis, the angle between the SMO orbital plane and the accretion disc $\iota_{\rm sd}$ is time dependent, so does the orbital period decay rate (equation 8). In addition to disc precession, we also consider a possible disc alignment process which is parametrized with an alignment time-scale $\tau_{\rm a}$ (equation 11). Therefore, four additional parameters $\{\alpha_{\rm ini}, \beta_{\rm ini}, \tau_{\rm p}, \tau_{\rm a}\}$ are introduced for describing the disc motion in this hypothesis (and the orbital period decay rate parameter $\dot{T}_{\rm obt}$ in $\mathcal{H}_0$ is replaced with $\dot{T}_{\rm obt,max}$).

From an SMO trajectory and disc motion, one can calculate the disc crossing times $t_{\rm crs}$, which we identify as the flare starting times. Specifically, we choose the disc crossing time as when the SMO crosses the upper disc surface or the lower disc surface depending on the observer direction, i.e. $r_{\rm crs}(\boldsymbol{n}_{\rm crs}\cdot\boldsymbol{n}_{\rm disc}) = H\ {\rm sign}(\boldsymbol{n}_{\rm obs}\cdot\boldsymbol{n}_{\rm disc})$. Without loss of generality, we fix the observer in the $x-z$ plane, i.e. the unit direction vector pointing to the observer is $\boldsymbol{n}_{\rm obs} = (\sin\theta_{\rm obs}, 0, \cos\theta_{\rm obs})$. The propagation times of different flares at different collision locations $r_{\rm crs}\boldsymbol{n}_{\rm crs}$ to the observer will also be different. Taking the light propagation delays into account, we find the flare starting time in the observer frame as

$$t_{\rm obs} = t_{\rm crs} + \delta t_{\rm geom} + \delta t_{\rm shap}\ , \tag{12}$$

where

$$\begin{aligned}\delta t_{\rm geom} &= -r_{\rm crs}\boldsymbol{n}_{\rm obs}\cdot\boldsymbol{n}_{\rm crs}\ ,\\ \delta t_{\rm shap} &= -2M_\bullet\log\left[r_{\rm crs}(1+\boldsymbol{n}_{\rm obs}\cdot\boldsymbol{n}_{\rm crs})\right]\ ,\end{aligned} \tag{13}$$

are corrections caused by different light path lengths and different Shapiro delays (Shapiro 1964), respectively. To summarize, our QPE timing model is written as $t_{\rm obs}^{(k)}(\Theta, \mathcal{H})$ in a short notation, where k is the index of observed flares, $\mathcal{H}$ is the hypothesis adopted, and Θ is the associated model parameters.

3.4 Bayesian framework

As discussed in previous analyses, it is possible that there are some physical processes that affect the QPE timing but are not included in our QPE timing model. Assuming the unmodelled advances or delays in the QPE timing follows a Gaussian distribution with variance $\sigma_{\rm sys}^2$, the likelihood of seeing data $d = \{t_0^{(k)}\}$ under hypothesis $\mathcal{H}$ with model parameters Θ is written as (see Paper II for a short derivation)

$$\mathcal{L}_{\rm timing}(d|\Theta,\mathcal{H}) = \prod_k \frac{1}{\sqrt{2\pi(\tilde{\sigma}(t_0^{(k)}))^2}}\exp\left\{-\frac{(t_{\rm obs}^{(k)}-t_0^{(k)})^2}{2(\tilde{\sigma}(t_0^{(k)}))^2}\right\}\ , \tag{14}$$

where $(\tilde{\sigma}(t_0^{(k)}))^2 = (\sigma(t_0^{(k)}))^2 + \sigma_{\rm sys}^2$ is the uncertainty contributed by both measurement error bars and unmodelled uncertainties. Note that Θ includes both the physical parameters introduced in the previous subsection and the systematic uncertainty parameter $\sigma_{\rm sys}$. Similar inference method has been widely used in the context of hierarchical test of general relativity with gravitational waves (Isi, Chatziioannou & Farr 2019).

For each QPE source, we apply both hypotheses $\mathcal{H}_{0,1}$ to the timing data of observed flares $t_0^{(k)}$, and perform model parameter inferences using the NESSAI (Williams 2021) algorithm within `Bilby` (Ashton et al. 2019) with the default settings, except more live points `nlive` = 2000 for better performance in the parameter inference. As we will see later, the data favoured hypothesis will be featured with higher evidence obtained from the Bayesian inference, and the hypothesis preference is quantified by the Bayes factor.

As a clean measurement of the SMBH mass from QPE timing data alone, we do not include any prior information about the SMBH mass informed by external measurements, e.g. commonly used $M_\bullet - \sigma_\star$ relations (Tremaine et al. 2002; Gültekin et al. 2009).

4 APPLICATIONS OF THE QPE TIMING METHOD

4.1 GSN 069

We first apply the comprehensive Bayesian framework to the well-studied QPE source, GSN 069, which has been extensively analysed in Papers I–III. In Table 1, we present the priors of model parameters used for orbital analyses in $\mathcal{H}_0$ and $\mathcal{H}_1$. In Fig. 3, the best-fitting EMRI trajectories of $\mathcal{H}_0$ and $\mathcal{H}_1$ are displayed along with the QPE light curves. The posterior corner plots of all model parameters are shown in Figs A1 and A2, respectively. The orbital parameters are constrained as

$$\begin{aligned} p &= 304^{+56}_{-134}\ M_\bullet\ ,\\ e &= 0.04^{+0.03}_{-0.02}\ , \quad (\mathcal{H}_0)\\ T_{\rm obt} &= 64.73^{+0.02}_{-0.03}\ {\rm ks}\ ,\\ \dot{T}_{\rm obt} &= -6.5^{+0.2}_{-0.2}\times10^{-5}\ ,\\ T_{\rm aps} &= 76^{+14}_{-34}\ {\rm d}\ , \end{aligned} \tag{15}$$

Table 1. Priors used for the orbital parameter inference of GSN 069 EMRI. Entries left blank in the $\pi(\Theta, \mathcal{H}_0)$ column indicate that the same prior values from the $\pi(\Theta, \mathcal{H}_1)$ column are imposed.

Θ	$\pi(\Theta, \mathcal{H}_1)$	$\pi(\Theta, \mathcal{H}_0)$
p [$M_\bullet$]	$\mathcal{U}[50, 500]$	
e	$\mathcal{U}[0, 0.9]$	
$\cos(\theta_{\rm min})$	$\mathcal{U}[0, 1]$	
$q_{r,\rm ini}$	$\mathcal{U}[0, 2\pi]$	
$q_{z,\rm ini}$	$\mathcal{U}[0, 2\pi]$	
$q_{\phi,\rm ini}$	$\mathcal{U}[0, 2\pi]$	
$T_{\rm obt}$ [ks]	$\mathcal{U}[60, 70]$	
a	$\mathcal{U}[0, 1]$	
$\theta_{\rm obs}$	$\mathcal{U}[0, \pi]$	$\mathcal{U}[0, \pi/2]$
$\alpha_{\rm ini}$	$\mathcal{U}[0, 2\pi]$	None
$\tau_{\rm p}$ [d]	$\mathcal{U}[1, 2000]$	None
$\beta_{\rm ini}$	$\mathcal{U}[0, \pi/2]$	None
$\tau_{\rm a}$ [d]	$\mathcal{U}[1, 2000]$	None
$\dot{T}_{\rm obt}$ [$\times 10^{-5}$]	None	$\mathcal{U}[-10, 0]$
$\dot{T}_{\rm obt,max}$ [$\times 10^{-5}$]	$\mathcal{U}[-10, 0]$	None
$\sigma_{\rm sys}$ [ks]	$\mathcal{U}[0, 2]$	

and

$$\begin{aligned} p &= 300^{+193}_{-48}\, M_\bullet\,, \\ e &= 0.04^{+0.02}_{-0.03}\,, \\ T_{\rm obt} &= 64.71^{+0.03}_{-0.05}\ {\rm ks}\,, \quad (\mathcal{H}_1) \\ \dot{T}_{\rm obt,max} &= -7.3^{+0.9}_{-2.2} \times 10^{-5}\,, \\ T_{\rm aps} &= 75^{+48}_{-12}\ {\rm d}\,, \\ \tau_{\rm p} &= 1288^{+664}_{-736}\ {\rm d}\,, \\ \tau_{\rm a} &= 1144^{+803}_{-810}\ {\rm d}\,, \end{aligned} \tag{16}$$

at 2σ confidence level, where the apsidal precession period is obtained from equation (2). The log Bayes factor between the two hypotheses is found to be

$$\log \mathcal{B}^1_0 = -1.9 \pm 0.2\,. \tag{17}$$

In Jeffreys' scale, disc precession in GSN 069 is substantially disfavoured.[2]

The Bayes factor itself may not be conclusive in excluding disc precession, since it depends on the parameter priors used. As a cross check, one can directly measure the disc precession period $\tau_{\rm p}$ from the QPE data. Consistent with the indication of the Bayes factor above, the disc precession period $\tau_{\rm p}$ is found to be even longer than the observation span (see equation 16), i.e. the disc precession is slow and has introduced little modulation on the QPE timing within the observation span. In addition, the two best-fitting trajectories in hypotheses $\mathcal{H}_0$ and $\mathcal{H}_1$ are quit similar, which is also consistent with slow disc precession in GSN 069. Longer monitoring is needed for accurately measuring such slow disc precession, and we will investigate disc precession measurement accuracy in more details in the following subsection.

The SMBH mass constraints in the data favoured hypothesis $\mathcal{H}_0$ is obtained from equations (1) and (2) as

$$\log_{10}(M_\bullet/{\rm M}_\odot) = 5.6^{+0.4}_{-0.1}\,, \qquad (\mathcal{H}_0) \tag{18}$$

at 2σ confidence level. This SMBH mass constraint is independent of and of significantly lower uncertainty than the constraint inferred from the $M_\bullet - \sigma_\star$ relation, $\log_{10}(M_\bullet/{\rm M}_\odot) = 6.0 \pm 1.0$ (at 2σ confidence level; Wevers et al. 2022).

In the data less favoured hypothesis $\mathcal{H}_1$, the apsidal precession and SMBH mass constraints are found to be

$$\log_{10}(M_\bullet/{\rm M}_\odot) = 5.6^{+0.1}_{-0.3}\,, \qquad (\mathcal{H}_1) \tag{19}$$

which is consistent with equation (18). This comparison also shows that the slow disc precession in GSN 069 has introduced weak modulation to the QPE timing. As a result, two different hypotheses yield consistent constraints of the SMBH mass.

GSN 069 represents a good example of dynamical measurement of SMBH masses with the QPE timing method. In addition to intrinsic EMRI orbital period and apsidal precession period, constraints of disc motion parameters are also obtained as side products.

4.2 Optimal observation strategy: SMBH mass measurement

In this subsection, we simulate different strategies of observing QPEs and evaluate their performances in measuring SMBH masses. As an example, we consider a mock QPE source that is similar to GSN 069 and eRO-QPE2, with source parameters $M_\bullet = 10^6\,{\rm M}_\odot$, $a = 0.9$, $p = 100M_\bullet$, and $e = 0.04$. The three dynamical time-scales are therefore $T_{\rm obt} = 31.5$ ks, $T_{\rm aps} = 12.1$ d, and $T_{\rm LT} = 202.5$ d. For convenience, we assume an equatorial disc and the injection values of full QPE timing model parameters are listed in Table 2. More general cases of EMRI + a precessing disc will be explored in a following subsection.

Using the osculating trajectory method described above, true flare starting times in the observer frame $t^{(k)}_{\rm obs,true}$ are calculated directly following equation (12). The observed flare starting times $t^{(k)}_0$ will be slightly different due to measurement noises,

$$t^{(k)}_0 = t^{(k)}_{\rm obs,true} + \delta t^{(k)}_0\,, \tag{20}$$

where $\delta t^{(k)}_0$ is randomly drawn from a Gaussian distribution with a mean value 0 and a standard deviation $\sigma(t^{(k)}_0)$. In this work, we fix the measurement uncertainty as $\sigma(t^{(k)}_0) = 100$ s.[3]

Different from traditional X-ray telescopes, CATCH consists of $\mathcal{O}(10^2)$ small satellites which enable uninterrupted long time-scale monitoring of multiple targets. A month long continuous monitoring of a number of particularly interesting sources is practical for CATCH (Li et al. 2023). As a reference, we first consider an uninterrupted observation epoch lasting for one apsidal precession period $T_{\rm aps} \approx 12$ d, then two different strategies of observation cadence and duration

[2]Miniutti et al. (2025) claimed that the superorbital modulation in the GSN 069 data is not likely from EMRI apsidal precession, but is from disc precession. Probably the most reliable way to test this claim is a simultaneous measurement of the EMRI apsidal precession period $T_{\rm aps}$ and the disc precession period $\tau_{\rm p}$ from the data assuming EMRI + a precessing disc ($\mathcal{H}_1$). However, the measurement result $\tau_{\rm p} \gg T_{\rm aps} \approx 76$ d (equation 16) supports the opposite: the disc precession is slow. NOTE that the $\tau_{\rm p}$ and $T_{\rm aps}$ constraints are measured from the GSN 069 data in the framework of EMRI + disc model, instead of an assumption. In Appendix B, we perform detailed O−C analyses for comparison and discuss possible sources of discrepancy in interpreting the superorbital modulation in the GSN 069 data.

[3]From *XMM–Newton* observations of eRO-QPE2, flare starting time uncertainties are found in the range of $\sim$ (30, 80) s (Zhou et al. 2024b). The current design of effective collecting area of a single CATCH satellite is 140 cm^2 in the keV range, which is smaller than that of *XMM–Newton* by a factor of $\sim$ 8. A simple scaling analysis shows that $\sim$ (80, 220) s or $\sim$ (60, 160) s uncertainties are expected if one or two CATCH satellites are used for eRO-QPE2 observations. We use 100 s as a fiducial value of flare starting time uncertainties in this work and it is straightforward to obtain model parameter constraints by simple scaling if a different resolution is assumed.

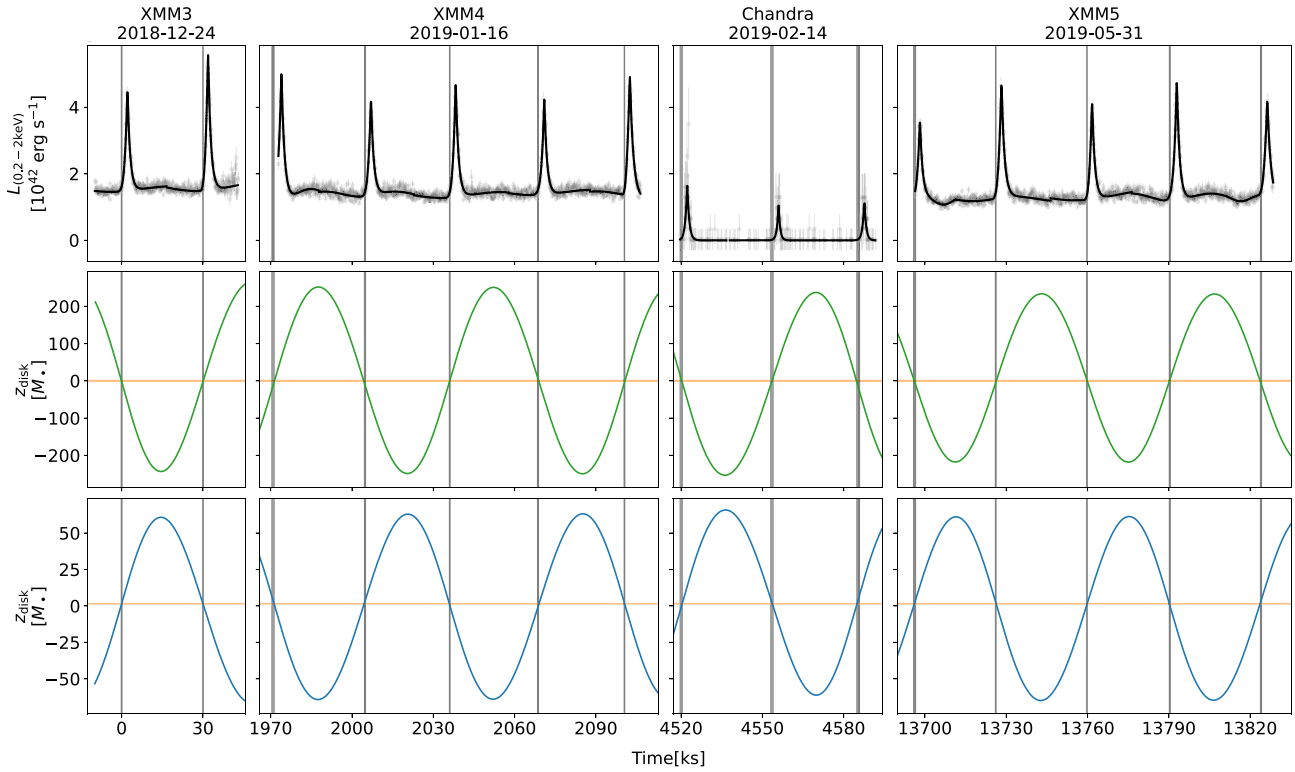

Figure 3. Top panel: light-curve data of GSN 069 along with the best-fitting EMRI trajectories, where the vertical bands are the inferred starting times $t_0^{(k)} \pm \sigma(t_0^{(k)})$ of the QPEs. Middle panel: distance to the disc mid-plane $z_{\mathrm{disc}}(t)$ of the best-fitting orbits for the disc precession and alignment hypothesis ($\mathcal{H}_1$), where the orange horizontal lines denote the disc surface $z = H$ and the verticals bands are the inferred starting times $t_0^{(k)} \pm \tilde{\sigma}(t_0^{(k)})$, with $\tilde{\sigma}(t_0^{(k)}) = \sqrt{(\sigma(t_0^{(k)}))^2 + \sigma_{\mathrm{sys}}^2}$. Bottom panel: same to the middle panel, but for the vanilla hypothesis ($\mathcal{H}_0$).

Table 2. Priors and the injection values of the QPE timing model parameters used for the simulations. Entries left blank in the $\pi(\Theta, \mathcal{H}_0)$ column indicate that the same prior values from the $\pi(\Theta, \mathcal{H}_1)$ column are imposed.

Θ	$\pi(\Theta, \mathcal{H}_1)$	$\pi(\Theta, \mathcal{H}_0)$	Injection values
p [$M_\bullet$]	$\mathcal{U}[50, 1000]$		100
e	$\mathcal{U}[0, 0.9]$		0.04
$\cos(\theta_{\mathrm{min}})$	$\mathcal{U}[0, 1]$		0.5
$q_{r,\mathrm{ini}}$	$\mathcal{U}[0, 2\pi]$		1.4π
$q_{z,\mathrm{ini}}$	$\mathcal{U}[0, 2\pi]$		1.6π
$q_{\phi,\mathrm{ini}}$	$\mathcal{U}[0, 2\pi]$		0.3π
T_{obt} [ks]	$\mathcal{U}[20, 40]$		31.5
a	$\mathcal{U}[0, 1]$		0.9
θ_{obs}	$\mathcal{U}[0, \pi]$	$\mathcal{U}[0, \pi/2]$	$\pi/3$
α_{ini}	$\mathcal{U}[0, 2\pi]$	None	0
τ_p [d]	$\mathcal{U}[1, 2000]$	None	7 & 20 & 150
β_{ini}	$\mathcal{U}[0, \pi/2]$	None	$\pi/7$
τ_a [d]	$\mathcal{U}[1, 2000]$	None	500
$\dot{T}_{\mathrm{obt}}$ [$\times 10^{-5}$]	None	$\mathcal{U}[-10, 0]$	-1
$\dot{T}_{\mathrm{obt,max}}$ [$\times 10^{-5}$]	$\mathcal{U}[-10, 0]$	None	-1
σ_{sys} [ks]	$\mathcal{U}[0, 2]$		0

of each observation epoch if the total amount of observation time is fixed as $T_{\mathrm{obs}} = 4$ d.

Strategy A. A single uninterrupted observation epoch lasting for one apsidal precession period $T_{\mathrm{aps}} \approx 12$ d.

Strategy B. Four observation epochs distributed randomly in 12 d, with each epoch lasting for 1 d.

Strategy C. Same to B, except for the epochs distributed randomly in ~ 50 d, mimicking existing QPE observations, e.g. observations of GSN 069 during 2018 December–2019 May (Fig. 1).

From mock observations of strategies A, B, and C, we infer model parameters as in the case of GSN 069. The model parameter priors used are listed in Table 2. The inferred values of the semilatus rectum p, eccentricity e, orbital period T_{obt}, apsidal precession period T_{aps} and SMBH mass $M_\bullet$ from the three strategies are summarized in Table 3. The best-fitting EMRI trajectories under the three strategies are shown in Fig. 4.

Specifically, we show the posteriors of the apsidal precession period T_{aps} in Fig. 5. It is of no surprise to find uninterrupted monitoring for a long time-scale (~ 12 d) in strategy A yields the tightest constraints on T_{aps} and consequently on the SMBH mass $M_\bullet$. If the total observation time is limited, observation cadence and duration of each observation epoch make a difference. Strategies B and C are similar except different observation cadence, which yield quite different T_{aps} constraints. Strategy B of high observation cadence also yields a reasonable constraint, wider than in strategy A by a factor of $\sim \sqrt{3}$. In contrast, strategy C of low observation cadence yields double-peak structure in the posterior of T_{aps}, a major peak located at the injection value and a minor one at roughly four times the injection value, in addition to two extra tiny peaks at twice and three times the injection value, respectively. For each peak, the fractional uncertainty $\delta T_{\mathrm{aps}}/T_{\mathrm{aps}}$ is comparable to in strategy B, due to comparable total observation time. This result is also consistent with the intuition that the phase information encoded in each observation epoch adds up 'coherently' if intervals

Table 3. Median values and 2σ uncertainties of semilatus rectum p, eccentricity e, orbital period $T_{\rm obt}$, apsidal precession period $T_{\rm aps}$, and SMBH mass $M_\bullet$ for the three strategies considered.

Strategy for mass measurement	p [$M_\bullet$]	e	$T_{\rm obt}$ [ks]	$T_{\rm aps}$ [d]	$\log_{10}(M_\bullet/{\rm M}_\odot)$
A	106^{+12}_{-16}	$0.04^{+0.00}_{-0.00}$	$31.5^{+0.03}_{-0.06}$	$12.9^{+1.5}_{-2.0}$	$5.96^{+0.11}_{-0.07}$
B	104^{+29}_{-18}	$0.04^{+0.01}_{-0.01}$	$31.5^{+0.04}_{-0.07}$	$12.6^{+3.5}_{-2.2}$	$5.98^{+0.12}_{-0.16}$
C (major/minor)	$107^{+19}_{-13}/378^{+34}_{-26}$	$0.05^{+0.02}_{-0.02}$	$31.5^{+0.03}_{-0.06}$	$13.1^{+2.4}_{-1.6}/46.0^{+4.1}_{-3.1}$	$5.95^{+0.08}_{-0.11}/5.13^{+0.05}_{-0.06}$

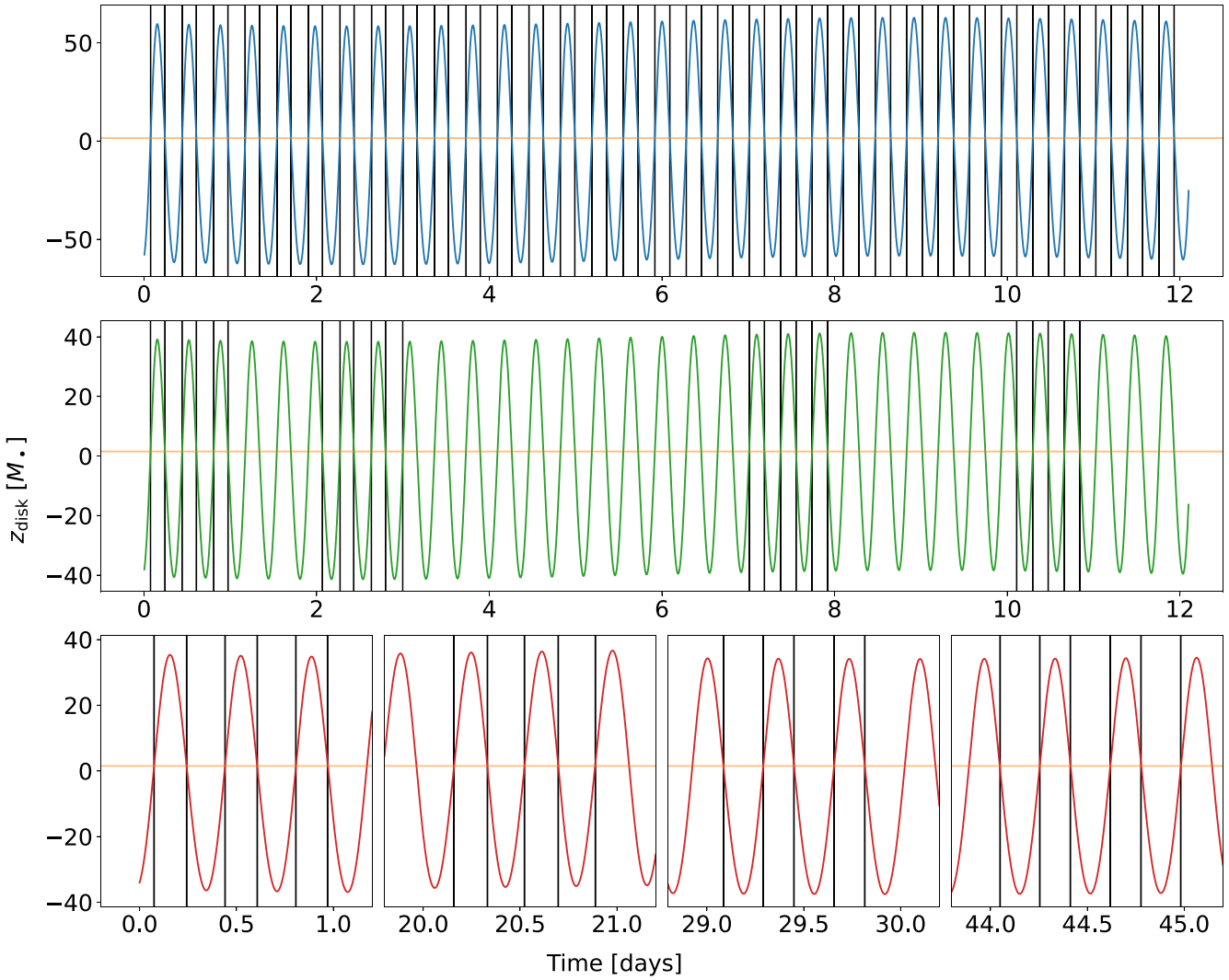

Figure 4. Best-fitting EMRI trajectories obtained with three different strategies, where $z_{\rm disc}(t)$ is the z-component. The vertical bands indicate the simulated data $t_0^{(k)} \pm \sigma(t_0^{(k)})$. The orange horizontal line marks the disc surface. Upper panel: strategy A. Middle panel: strategy B. Lower panel: strategy C.

between consecutive observations is short ($\ll T_{\rm aps}$) as in strategy B. Otherwise, multiple peaks in the posterior may show up as in strategy C.[4]

For the purpose of precise measurement of SMBH masses from QPE timing, the optimal strategy is clearly strategy A, which consists of a single observation epoch that spans an entire apsidal precession period $T_{\rm aps}$. However, QPE sources exhibit a wide range of $T_{\rm aps}$ from tens to hundreds of of days. For sources of particular interest, such as eRO-QPE2 with $T_{\rm aps} \sim 1$ month, uninterrupted long-term monitoring over one full $T_{\rm aps}$ is feasible for CATCH. Nevertheless, this approach becomes impractical for sources with longer $T_{\rm aps}$. A more practical alternative exemplified by strategy B is to divide the limited total observation time into $N \approx T_{\rm obs}/(2T_{\rm obt})$ separate epochs, ensuring that each epoch captures at least $\gtrsim 3$ QPE flares. To properly sample the phase information of apsidal precession, these epochs should be quasi-uniformly distributed within one $T_{\rm aps}$, as exemplified in strategy B.

[4]Multiple peaks in the posterior may pose a challenge for some samplers. The sampler NESSAI with a large number of live points used in this work seem to properly sample all the peaks (see Fig. 5 for example).

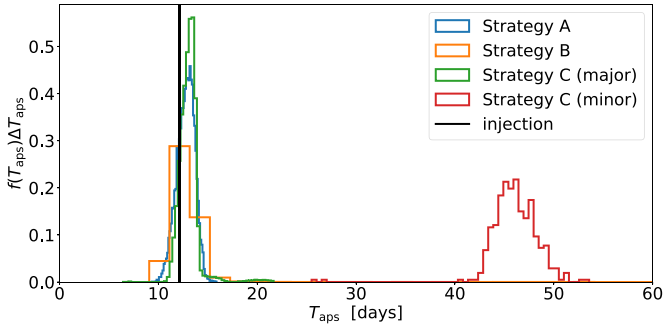

Figure 5. Probability distributions $f(T_{aps})\Delta T_{aps}$ of the apsidal precession period T_{aps} obtained from three different observation strategies, where ΔT_{aps} is the bin size.

4.3 Disc motion

In the previous subsection, we have applied the QPE timing method to mock QPE data assuming an equatorial disc ($\mathcal{H}_0$). As elaborated in Section 3.2, the QPE timing method is flexible in incorporating the component of disc motion ($\mathcal{H}_1$). Both hypotheses can be adopted in analysing the QPE timing data and the support to one hypothesis to another by data can be quantified in three ways as shown in Section 4.1: the best-fitting models in the two hypotheses, the Bayes factor $\mathcal{B}^1_0$, and the constraint of disc precession period τ_p in $\mathcal{H}_1$. For demonstrating the robustness of the QPE timing method for more general cases where the disc is precessing and aligning, we generate three more sets of mock QPE data assuming a ~ 12 d long observation of an EMRI + disc system with same disc motion parameters $\alpha_{ini} = 0$, $\beta_{ini} = \pi/7$, $\tau_a = 500$ d and different disc precession periods $\tau_p = 7$, 20, and 150 d, respectively. All other injection parameters remain the same as in the previous subsection (Table 2). For comparison, we also generate a set mock data assuming an equatorial disc as in previous subsection.

We fit each set of mock data with the EMRI + disc model with hypotheses $\mathcal{H}_0$ (an equatorial disc) and $\mathcal{H}_1$ (a precessing disc), respectively. The priors used in the Bayesian inference are listed in Table 2 and the constraints on a fraction of model parameters obtained are summarized in Table 4. We summarize the analysis results as follows.

Fast disc precession with $\tau_p = 7$ or 20 d: the best-fitting EMRI trajectories with the two hypotheses $\mathcal{H}_{0,1}$ are shown in Figs C1 and C2, from which, the disc-precessing hypothesis $\mathcal{H}_1$ is clearly favoured over the equatorial disc hypothesis $\mathcal{H}_0$. This intuition is also supported by large log Bayes factors $\log \mathcal{B}^1_0$ summarized in Table 4. With the data favoured hypothesis $\mathcal{H}_1$, it is of no surprise to find that all the physical parameters, including the semilatus rectum p, eccentricity e, orbital period T_{obt}, apsidal precession period T_{aps}, SMBH mass $M_\bullet$, and the disc precession period τ_p are correctly recovered and tightly constrained (Table 4). The other hypothesis $\mathcal{H}_0$ with a conflicting assumption is strongly disfavoured by the mock data according to both the not well-behaved best-fitting trajectory and the log Bayes factor.

With hypothesis $\mathcal{H}_0$, the EMRI orbital period T_{obt} is still tightly constrained since they are mostly constrained by the alternating long-short pattern in the recurrence times, therefore is not strongly affected by the model assumption on the disc motion, while the apsidal precession alone cannot properly fit two different superorbital modulations introduced by both the apsidal precession and the disc precession, therefore the apsidal precession period $T_{aps}(\propto p)$ is not well constrained.

Slow disc precession with $\tau_p = 150$ d: the best-fitting EMRI trajectories with the two hypotheses $\mathcal{H}_{0,1}$ are shown in Fig. C3. The two best-fitting trajectories are quite similar, because the slow disc precession makes little difference to the QPE timing during the relatively short observation span. Consequently, the disc precession period τ_p in $\mathcal{H}_1$ is barely constrained, where no disc precession ($\tau_p \to \infty$) is also compatible with the mock data, and the upper end of the 2σ credible interval obtained is in fact determined by the prior imposed. Consistent with the resemblance of the two trajectories, the log Bayes factor between the two hypotheses $\log \mathcal{B}^1_0 = 0.4 \pm 0.2$ also shows that there is no preference for one hypothesis over another from the mock data. As a result, the model parameter constraints in the two different hypotheses are also found to be similar.

Equatorial disc ($\tau_p = \infty$): the best-fitting EMRI trajectories under the two hypotheses $\mathcal{H}_0$ and $\mathcal{H}_1$ are shown in Fig. C4. Similar to the slow precession case, the two trajectories are close due to the absence of disc-induced modulation. In hypothesis $\mathcal{H}_1$, the precession period τ_p remains unconstrained, with the posterior dominated by the prior imposed. It is natural to find a log Bayes factor $\log \mathcal{B}^1_0 = -1.2 \pm 0.2$, which represents substantial preference for the true hypothesis $\mathcal{H}_0$. This case is quite similar to GSN 069.

The injection and recovery experiments demonstrate that EMRI apsidal and disc precessions are not degenerate, both of which can be correctly recovered from QPE timing data, no matter the disc precession is fast, slow or absent. In particular, for fast precessing discs ($\tau_p \lesssim$ observation span), the disc precession period is well constrained and the true hypothesis $\mathcal{H}_1$ is strongly favored according to the log Bayes factor $\log \mathcal{B}^1_0$. With a wrong hypothesis $\mathcal{H}_0$, the best-fitting model prediction is clearly off the data simply because apsidal precession alone cannot explain modulations in QPE timing data from both apsidal and disc precessions.

For a slowly precessing disc ($\tau_p \gg$ observation span), the disc precession period τ_p in $\mathcal{H}_1$ is unconstrained, simply because disc-induced superorbital modulations are negligible within the observation window. As a result, two best-fitting trajectories in the two hypotheses are found to be quite similar, and there is no preference for equatorial disc precession hypothesis $\mathcal{H}_0$ over $\mathcal{H}_1$ according to the log Bayes factor.

For an equatorial disc, the disc precession period τ_p in $\mathcal{H}_1$ is again unconstrained. It is natural to find quite similar best-fitting model predictions in the two hypotheses. The true hypothesis $\mathcal{H}_0$ is favoured according to the log Bayes factor.

Table 4. Median values and 2σ uncertainties of semilatus rectum p, eccentricity e, orbital period $T_{\rm obt}$, apsidal precession period $T_{\rm aps}$, disc precession period $\tau_{\rm p}$, and SMBH mass $M_\bullet$ for different injections and hypotheses.

Injection	Hypothesis	$p\ [M_\bullet]$	e	$T_{\rm obt}$ [ks]	$T_{\rm aps}$ [d]	$\tau_{\rm p}$ [d]	$\log_{10}(M_\bullet/{\rm M}_\odot)$	$\log \mathcal{B}^1_0$
Precessing disc	$\mathcal{H}_0$	604^{+376}_{-471}	$0.08^{+0.16}_{-0.07}$	$31.6^{+0.06}_{-0.06}$	$73.6^{+45.8}_{-57.4}$		$4.82^{+0.99}_{-0.32}$	
($\tau_{\rm p}=7$ d)	$\mathcal{H}_1$	107^{+13}_{-10}	$0.04^{+0.01}_{-0.01}$	$31.5^{+0.04}_{-0.03}$	$13.0^{+1.6}_{-1.2}$	$7.1^{+0.1}_{-0.1}$	$5.95^{+0.06}_{-0.07}$	213.2 ± 0.2
	$\mathcal{H}_0$	603^{+379}_{-490}	$0.06^{+0.19}_{-0.06}$	$31.4^{+0.06}_{-0.06}$	$73.0^{+45.9}_{-59.5}$		$4.82^{+1.10}_{-0.32}$	
($\tau_{\rm p}=20$ d)	$\mathcal{H}_1$	112^{+44}_{-24}	$0.05^{+0.02}_{-0.02}$	$31.5^{+0.17}_{-0.14}$	$13.6^{+5.5}_{-3.0}$	$19.8^{+21.7}_{-5.7}$	$5.93^{+0.16}_{-0.22}$	194.0 ± 0.2
	$\mathcal{H}_0$	108^{+20}_{-17}	$0.04^{+0.01}_{-0.00}$	$31.5^{+0.03}_{-0.06}$	$13.2^{+2.5}_{-2.1}$		$5.94^{+0.11}_{-0.11}$	
($\tau_{\rm p}=150$ d)	$\mathcal{H}_1$	109^{+18}_{-12}	$0.04^{+0.01}_{-0.01}$	$31.5^{+0.02}_{-0.02}$	$13.3^{+2.2}_{-1.5}$	1250^{+704}_{-857}	$5.94^{+0.08}_{-0.10}$	0.4 ± 0.2
Equatorial disc	$\mathcal{H}_0$	Same as the strategy A in Table 3						
($\tau_{\rm p}=\infty$)	$\mathcal{H}_1$	106^{+11}_{-11}	$0.04^{+0.01}_{-0.01}$	$31.5^{+0.02}_{-0.03}$	$12.9^{+1.3}_{-1.3}$	1181^{+770}_{-849}	$5.96^{+0.07}_{-0.06}$	-1.2 ± 0.2

4.4 Optimal observation strategy: SMBH spin measurement

Similar to the apsidal precession, Lense–Thirring precession of the EMRI orbital plane in the Kerr space–time also introduces a superorbital modulation to the QPE recurrence times. In general, the Lense–Thirring precession period $T_{\rm LT}$ is much longer than both the orbital period $T_{\rm obt}$ and the apsidal precession period $T_{\rm aps}$. Uninterrupted monitoring of QPE sources for a long period of time $\sim T_{\rm LT}$ seems impractical even for CATCH. To demonstrate the feasibility of the QPE timing method in measuring the SMBH spin with a limited amount of observation time $T_{\rm obs}\ll T_{\rm LT}$, we fix $T_{\rm obs}=15$ d and simulate the following two observation strategies.

Strategy I. 15 observation epochs with each epoch lasting for 1 d and distributed within $T_{\rm LT}$ in a quasi-uniform way.

Standard II. 5 observation epochs with each epoch lasting for 3 d and distributed within $T_{\rm LT}$ in a quasi-uniform way.

We perform the Bayesian analysis as in the case of SMBH mass measurement simulations. The inferred values of the semilatus rectum p, eccentricity e, orbital period $T_{\rm obt}$, apsidal precession period $T_{\rm aps}$, Lense–Thirring precession period $T_{\rm LT}$, SMBH mass $M_\bullet$, and SMBH spin a from the two strategies are summarized in Table 5. The best-fitting EMRI trajectories under the three strategies are shown in Fig. 6.

Although observations of low cadence are not able to resolve apsidal precession in strategy C, more observations as in strategy I, make a difference. If enough amount of separated observation epochs are distributed within one $T_{\rm LT}$, strategy I demonstrates that $T_{\rm LT}$ can be resolved, which in turn improves the resolution of $T_{\rm aps}$. Meanwhile, the strategy II with an even lower observation cadence yet longer single epoch duration within one $T_{\rm LT}$ achieves the same precision of $M_\bullet$ and a measurement as in strategy I. Both strategies I and II reduce the 2σ uncertainty of $\log_{10}(M_\bullet)$ by an order of magnitude compared to strategies A–C. The SMBH spin a is also well constrained with comparable 2σ uncertainties <0.1 in both strategies I and II. Strategy I with higher cadence yields tighter constraints on a fraction of model parameters (e, $T_{\rm obt}$, $T_{\rm aps}$) than in strategy II.

A similar idea has also been proposed for measuring the Sgr A* SMBH spin by tracing S stars (Zhang, Lu & Yu 2015). For the star S2, the Lense–Thirring precession is out of reach of the current astrometry (Genzel, Eisenhauer & Gillessen 2024). A star moving around the Sgr A* on a tighter orbit is desired for detecting the SMBH spin from Lense–Thirring precession (Waisberg et al. 2018).

5 SUMMARY AND DISCUSSIONS

More and more analyses show that (at least a fraction of) QPEs are sourced by quasi-periodic collisions between SMOs and accretion discs of SMBHs. As a result, the QPE timing data encode rich information of the EMRI trajectory, including the orbital period $T_{\rm obt}$, the apsidal precession period $T_{\rm aps}$ and the Lense–Thirring precession period $T_{\rm LT}$, If these periods are extracted from QPE timing data, one then can robustly measure the SMBH mass and spin. We name this dynamical measurement method as the QPE timing method, which is in the same spirit of measuring the Sagittarius A* SMBH mass by tracing individual stars around the SMBH (Schödel et al. 2002; Ghez et al. 2005; Gillessen et al. 2009; GRAVITY Collaboration 2018). The QPE timing method can be applied to a much broader range of SMBHs since there is no need to spatially resolve the orbits of individual stars.

To implement the QPE timing method, we constructed a comprehensive Bayesian inference framework in which one can reconstruct the EMRI trajectory (and the disc motion), consequently measure the SMBH parameters from QPE timing data.

As an example, we first applied the QPE timing method to the well-studied QPE source GSN 069, analysing its orbital parameters under different hypotheses in the Bayesian inference framework. In the disc precession hypothesis $\mathcal{H}_1$, the disc precession period $\tau_{\rm p}$ is found to be longer than the observation span, therefore introduces negligible modulation to the QPE timing. This observation is also supported by similar best-fitting EMRI trajectories in $\mathcal{H}_1$ and in $\mathcal{H}_0$ (an equatorial disc). Consistent with this observation, the log Bayes factor (equation 17) between two different hypotheses also represents substantial preference for $\mathcal{H}_0$. In the data favoured hypothesis $\mathcal{H}_0$, the SMBH mass is tightly constrained (equation 18), with an uncertainty lower than intrinsic uncertainties of $M_\bullet-\sigma_\star$ relations. The other hypothesis $\mathcal{H}_1$ yields similar model parameter constraints.

To further demonstrate the robustness of the QPE timing method in the presence of disc motion, we generated additional mock QPE data sets assuming a precessing and aligning disc with a wide range of precession periods, and analysed them under both hypotheses $\mathcal{H}_0$ and $\mathcal{H}_1$. As a result, we find that $\mathcal{H}_1$ is strongly favoured, in terms of Bayes factor, trajectory best-fits and the constraint of disc precession period $\tau_{\rm p}$, when the disc is precessing rapidly. In the case of a slowly precessing disc with $\tau_{\rm p}$ much longer than the observation span, the disc precession period $\tau_{\rm p}$ is unconstrained; neither hypothesis is strongly preferred according to the log Bayes factor; however, both yield similar accurate recovery of EMRI orbital parameters. In the case of an equatorial disc, the disc precession period $\tau_{\rm p}$ is unconstrained and the precessing disc hypothesis $\mathcal{H}_1$

Table 5. Median values and 2σ uncertainties of semilatus rectum p, eccentricity e, orbital period $T_{\rm obt}$, apsidal precession period $T_{\rm aps}$, Lense–Thirring precession period $T_{\rm LT}$, SMBH mass $M_\bullet$, and SMBH spin a for the two strategies considered.

Strategy for spin measurement	p $[M_\bullet]$	e	$T_{\rm obt}$ [ks]	$T_{\rm aps}$ [d]	$T_{\rm LT}$ [d]	$\log_{10}(M_\bullet/{\rm M}_\odot)$	a
I	100^{+1}_{-1}	$0.04^{+0.005}_{-0.005}$	$31.5^{+0.005}_{-0.004}$	$12.1^{+0.1}_{-0.1}$	203^{+22}_{-14}	$6.00^{+0.01}_{-0.01}$	$0.89^{+0.07}_{-0.08}$
II	101^{+3}_{-1}	$0.04^{+0.01}_{-0.01}$	$31.5^{+0.01}_{-0.01}$	$12.2^{+0.3}_{-0.2}$	213^{+24}_{-13}	$6.00^{+0.01}_{-0.02}$	$0.86^{+0.06}_{-0.08}$

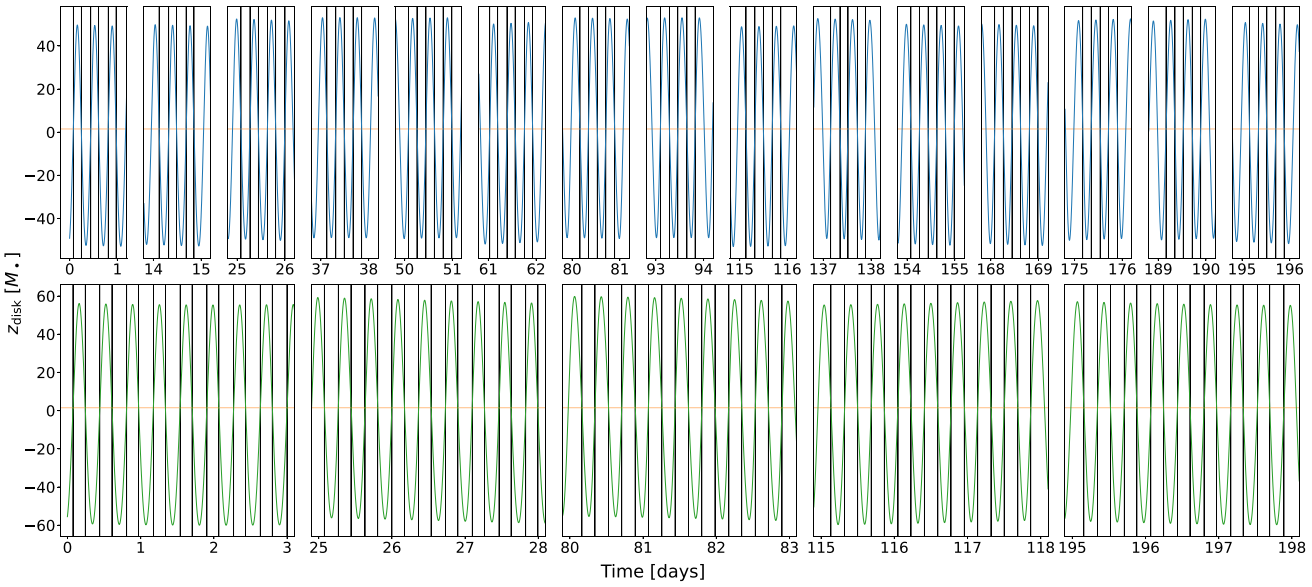

Figure 6. Same to Fig. 4 except for strategies to SMBH spin measurement. Upper panel: strategy I. Lower panel: strategy II.

is disfavored according to the log Bayes factor; EMRI orbital parameters are correctly recovered in both hypotheses. Notably, these tests confirm that EMRI motion and disc motion are not degenerate in QPE timing data: the underlying EMRI dynamics can be reliably inferred no matter the disc precession is fast, slow or absent. These examples demonstrate the feasibility of the QPE timing method in reconstructing the EMRI trajectory and the disc motion.

The QPE timing method opens up the possibility for precision measurement of SMBHs, though the current bottleneck is the limited X-ray observation resources available. The multitarget X-ray telescope under construction, CATCH (Li et al. 2023), will hopefully be the solution to the bottleneck of X-ray follow-up observation. First, CATCH will allow comprehensive X-ray monitoring of a large sample of optical TDEs in the era of the Rubin Observatory Legacy Survey of Space and Time (Ivezić et al. 2019) and the Wide Field Survey Telescope (Wang et al. 2023), and thus the discovery of a large number of QPEs following TDEs. In fact, it is impractical to follow all TDEs that will be discovered in the near future even for CATCH. This is not necessary either. There is emerging evidence suggesting that QPEs are not equally associated with all TDEs, yet they occur at a much higher rate in recently faded AGNs (Jiang & Pan 2025). This preferred subset of TDEs can be identified by their bright infrared echoes from torus remnant (Wu et al. 2025) or by the presence of extended emission-line regions in their host galaxies (Xiong et al. 2025). Accurate measurements of even a small number of SMBHs with QPE timing data are valuable, e.g. in calibrating traditional mass measurement methods in the low-mass range. In addition, different from traditional X-ray telescopes, CATCH consists of $\sim 10^2$ small satellites, a small number of which can be fully reserved for TDE follow-up and QPE monitoring. Refined observations can then be made for the QPE targets.

In this work, we explored different observation strategies for accurately measuring SMBH masses from QPE timing in the CATCH era. In general, the apsidal precession period $T_{\rm aps}$ is much longer than the orbital period $T_{\rm obt}$, therefore is harder to be accurately measured. As a result, the mass $M_\bullet$ measurement precision is mainly determined by the measurement precision of the apsidal precession period, with

$$\frac{\delta M_\bullet}{M_\bullet} \approx \frac{3}{2}\frac{\delta T_{\rm aps}}{T_{\rm aps}} \,. \tag{21}$$

For particularly interesting QPE sources, the design of CATCH enables uninterrupted long-term (say $\sim$ 1 month) monitoring. This will of course be the optimal strategy for precision measurement of SMBH masses. For general QPE sources, we may allocate less total amount of observation time $T_{\rm obs}$, and divide the total observation time into $N \approx T_{\rm obs}/(2T_{\rm obt})$ epochs that are distributed in a quasi-uniform way within one apsidal precession period $T_{\rm aps}$. In this way, each observation epoch guarantees to detect $\gtrsim 3$ eruptions, and the apsidal precession information encoded in different epochs adds up 'coherently', therefore enables an optimal measurement of $T_{\rm aps}$ given a limited amount of total observation time.

In addition to apsidal precession of the EMRI, a misaligned and precessing disc is also possible to introduce superorbital modulations to the QPE timing. In this case, the disc motion information may also be extracted from the QPE data as demonstrated via the injection and inference experiments in Section 3.2.

The same strategy works for measuring the SMBH spin using the QPE timing method. The only difference is that a even longer timescale $T_{\rm LT}$ matters, which takes more observation time to be measured. The spin measurement precision is up to the measurement precision of the Lense–Thirring precession period $T_{\rm LT}$ with

$$\frac{\delta a}{a} \approx \frac{\delta T_{\rm LT}}{T_{\rm LT}} \,. \tag{22}$$

In practice, the apsidal precession period $T_{\rm aps}$ and the Lense–Thirring precession period $T_{\rm LT}$ are unknown *a priori*. Therefore, the observation strategy and the model parameter inference can only be updated iteratively.

ACKNOWLEDGEMENTS

We thank the anonymous referee for helpful comments. We thank Yue Liao for helping making the schematic picture in Fig. 2. This work is supported by the Strategic Priority Research Program of the Chinese Academy of Sciences (XDB0550200), the National Natural Science Foundation of China (grants 12192221 and 12393814), and the China Manned Space Project.

DATA AVAILABILITY

ObsIDs of the three *XMM–Newton* observations are 0823680101, 0831790701, and 0851180401. The *Chandra* observation (ObsID:22096) of GSN 069 at 2019 February 14 can be obtained by the *Chandra X-ray Observatory*, contained in the Chandra Data Collection (CDC) 368 doi:10.25574/cdc.368.

REFERENCES

Abuter R. et al., 2024, Nature, 627, 281
Arcodia R. et al., 2021, Nature, 592, 704
Arcodia R. et al., 2022, A&A, 662, A49
Arcodia R. et al., 2024a, A&A, 684, A64
Arcodia R. et al., 2024b, A&A, 684, L14
Arcodia R. et al., 2024c, A&A, 690, A80
Ashton G. et al., 2019, ApJS, 241, 27
Burke C. J. et al., 2021, Science, 373, 789
Bykov S., Gilfanov M., Sunyaev R., Medvedev P., 2025, MNRAS, 540, 30
Chakraborty J. et al., 2024, ApJ, 965, 12
Chakraborty J. et al., 2025, ApJ, 983, L39
Chakraborty J., Kara E., Masterson M., Giustini M., Miniutti G., Saxton R., 2021, ApJ, 921, L40
den Brok M. et al., 2015, ApJ, 809, 101
Evans P. A. et al., 2023, Nat. Astron., 7, 1368
Ferrarese L., Merritt D., 2000, ApJ, 539, L9
Franchini A. et al., 2023, A&A, 675, A100
Fujita R., Hikida W., 2009, Class. Quantum Gravity, 26, 135002
Gebhardt K. et al., 2000, ApJ, 539, L13
Genzel R., Eisenhauer F., Gillessen S., 2024, A&AR, 32, 3
Ghez A. M., Salim S., Hornstein S. D., Tanner A., Lu J. R., Morris M., Becklin E. E., Duchêne G., 2005, ApJ, 620, 744
Gilbert O., Ruan J. J., Eracleous M., Haggard D., Runnoe J. C., 2024, ApJ, preprint (arXiv:2409.10486)
Gillessen S., Eisenhauer F., Trippe S., Alexander T., Genzel R., Martins F., Ott T., 2009, ApJ, 692, 1075
Giustini M. et al., 2024, A&A, 692, A15
Giustini M., Miniutti G., Saxton R. D., 2020, A&A, 636, L2
Götz D. et al., 2009, in Meegan C., Kouveliotou C., Gehrels N., eds, AIP Conf. Proc. Vol. 1133, Gamma-ray Burst: Sixth Huntsville Symposium. AIP, New York, p. 25
GRAVITY Collaboration, 2018, A&A, 615, L15
Gravity Collaboration, 2018, Nature, 563, 657
Greene J. E., Strader J., Ho L. C., 2020, ARA&A, 58, 257
Gültekin K. et al., 2009, ApJ, 698, 198
Guolo M. et al., 2024, Nat. Astron., 8, 347
Heckman T. M., Best P. N., 2014, ARA&A, 52, 589
Hernández-García L. et al., 2025, Nat. Astron., 9, 895
Ho L. C., Kim M., 2014, ApJ, 789, 17
Huang Y. et al., 2024, Exp. Astron., 58, 16
Isi M., Chatziioannou K., Farr W. M., 2019, Phys. Rev. Lett., 123, 121101
Ivezić Ž. et al., 2019, ApJ, 873, 111
Jiang N., Pan Z., 2025, ApJ, 983, L18
Kaur K., Rom B., Sari R., 2025, ApJ, 980, 150
Kejriwal S., Witzany V., Zajacek M., Pasham D. R., Chua A. J. K., 2024, MNRAS, 532, 2143
Kormendy J., Ho L. C., 2013, ARA&A, 51, 511
Kormendy J., Richstone D., 1995, ARA&A, 33, 581
Li P. et al., 2023, Exp. Astron., 55, 447
Linial I., Metzger B. D., 2023, ApJ, 957, 34
Linial I., Metzger B. D., 2024a, ApJ, 973, 101
Linial I., Metzger B. D., 2024b, ApJ, 963, L1
Linial I., Quataert E., 2024, MNRAS, 527, 4317
McConnell N. J., Ma C.-P., 2013, ApJ, 764, 184
McHardy I. M., Koerding E., Knigge C., Uttley P., Fender R. P., 2006, Nature, 444, 730
Miniutti G. et al., 2019, Nature, 573, 381
Miniutti G. et al., 2025, A&A, 693, A179
Miniutti G., Giustini M., Arcodia R., Saxton R. D., Chakraborty J., Read A. M., Kara E., 2023b, A&A, 674, L1
Miniutti G., Giustini M., Arcodia R., Saxton R. D., Read A. M., Bianchi S., Alexander K. D., 2023a, A&A, 670, A93
Nicholl M. et al., 2024, Nature, 8035, 804
Pan H.-W., Yuan W., Zhou X.-L., Dong X.-B., Liu B., 2015, ApJ, 808, 163
Pasham D., Kejriwal S., Coughlin E., Witzany V., Chua A. J. K., Zajaček M., Wevers T., Ajay Y., 2024a, ApJ, preprint (arXiv:2411.00289)
Pasham D. R. et al., 2024b, ApJ, 963, L47
Peterson B. M. et al., 2005, ApJ, 632, 799
Peterson B. M., 2014, Space Sci. Rev., 183, 253
Ponti G., Papadakis I., Bianchi S., Guainazzi M., Matt G., Uttley P., Bonilla N. F., 2012, A&A, 542, A83
Scheuer P. A. G., Feiler R., 1996, MNRAS, 282, 291
Schmidt W., 2002, Class. Quantum Gravity, 19, 2743
Schödel R. et al., 2002, Nature, 419, 694
Shapiro I. I., 1964, Phys. Rev. Lett., 13, 789
Shen Y., 2013, Bull. Astron. Soc. India, 41, 61
Sun L., Shu X., Wang T., 2013, ApJ, 768, 167
Tagawa H., Haiman Z., 2023, MNRAS, 526, 69
Tremaine S. et al., 2002, ApJ, 574, 740
van de Meent M., 2020, Class. Quantum Gravity, 37, 145007
Vurm I., Linial I., Metzger B. D., 2025, ApJ, 983, 40
Waisberg I. et al., 2018, MNRAS, 476, 3600
Wang T. et al., 2023, Sci. China Phys. Mech. Astron., 66, 109512
Wang Y., Zhu Z., Lin D. N. C., 2024, MNRAS, 528, 4958
Wevers T. et al., 2024, ApJ, 970, L23
Wevers T., Pasham D. R., Jalan P., Rakshit S., Arcodia R., 2022, A&A, 659, L2
Williams M. J., 2021, nessai: Nested Sampling with Artificial Intelligence. Zenodo, doi:10.5281/zenodo.4550693
Woo J.-H., Cho H., Gallo E., Hodges-Kluck E., Le H. A. N., Shin J., Son D., Horst J. C., 2019, Nat. Astron., 3, 755
Wu M., Jiang N., Zhu J., Luo D., Dou L., Wang T., 2025, ApJ, 988, L77
Xian J., Zhang F., Dou L., He J., Shu X., 2021, ApJ, 921, L32
Xiong Y., Jiang N., Pan Z., Hao L., Li Z., 2025, ApJ, 989, 49
Yao P. Z., Quataert E., Jiang Y.-F., Lu W., White C. J., 2025, ApJ, 978, 91
Zanazzi J. J., Lai D., 2019, MNRAS, 487, 4965
Zhang F., Lu Y., Yu Q., 2015, ApJ, 809, 127
Zhou C., Huang L., Guo K., Li Y.-P., Pan Z., 2024a, Phys. Rev. D, 109, 103031

Zhou C., Zeng Y., Pan Z., 2025, ApJ, 985, 242
Zhou C., Zhong B., Zeng Y., Huang L., Pan Z., 2024b, Phys. Rev. D, 110, 083019

APPENDIX A: POSTERIOR CORNER PLOTS OF GSN 069

In the section, we include posterior corner plots of model parameters in hypotheses $\mathcal{H}_0$ and $\mathcal{H}_1$ for analysing QPE timing data of GSN 069.

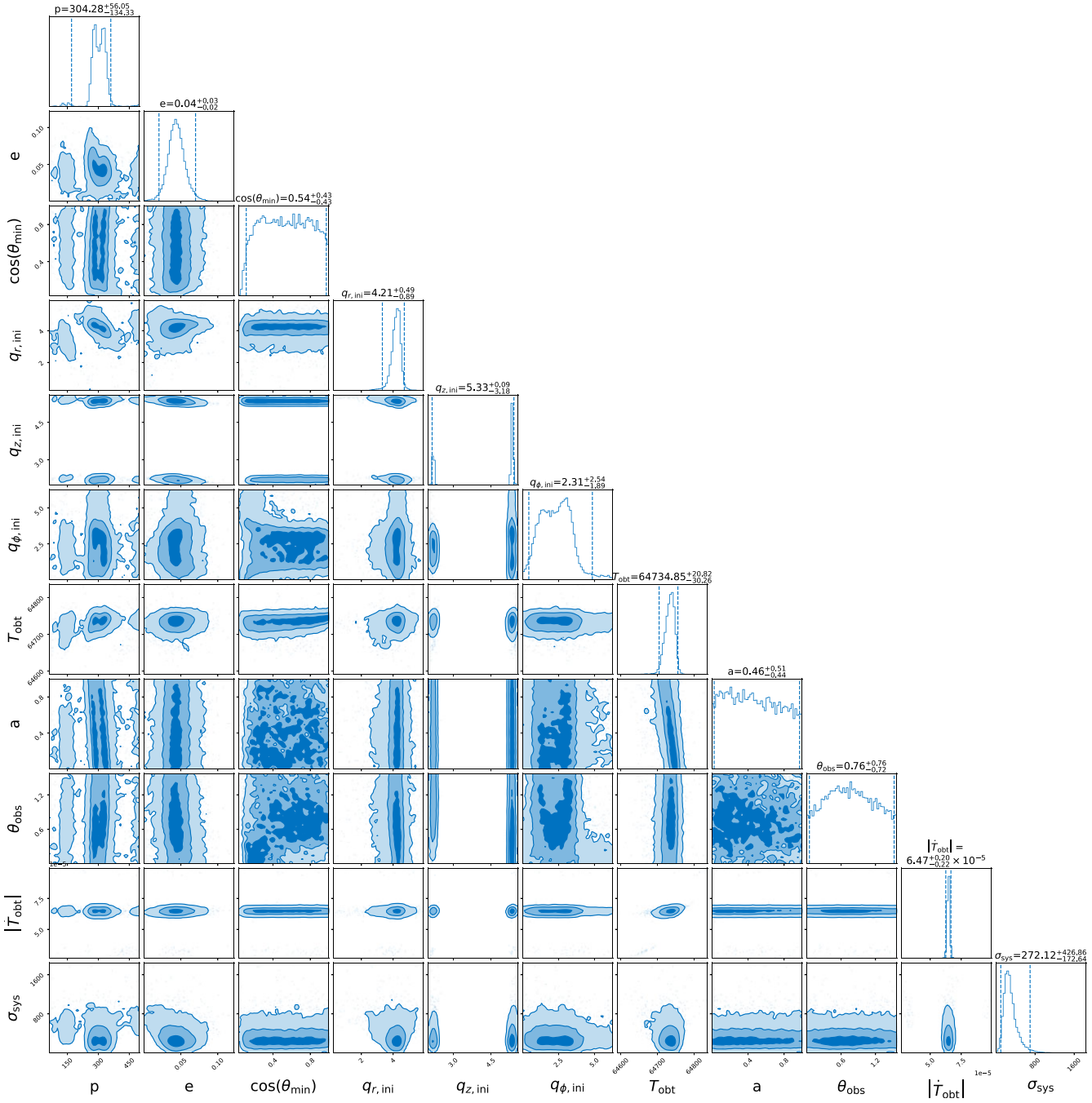

Figure A1. The posterior corner plot of model parameters for GSN 069 with the vanilla hypothesis ($\mathcal{H}_0$): $p[M_\bullet]$, e, $\cos\theta_{\rm min}$, $q_{r,\rm ini}$, $q_{z,\rm ini}$, $q_{\phi,\rm ini}$, $T_{\rm obt}$[s], a, $\theta_{\rm obs}$, $\dot{T}_{\rm obt}[\times 10^{-5}]$, $\sigma_{\rm sys}$[s], where each pair of vertical lines denotes the 2σ confidence level.

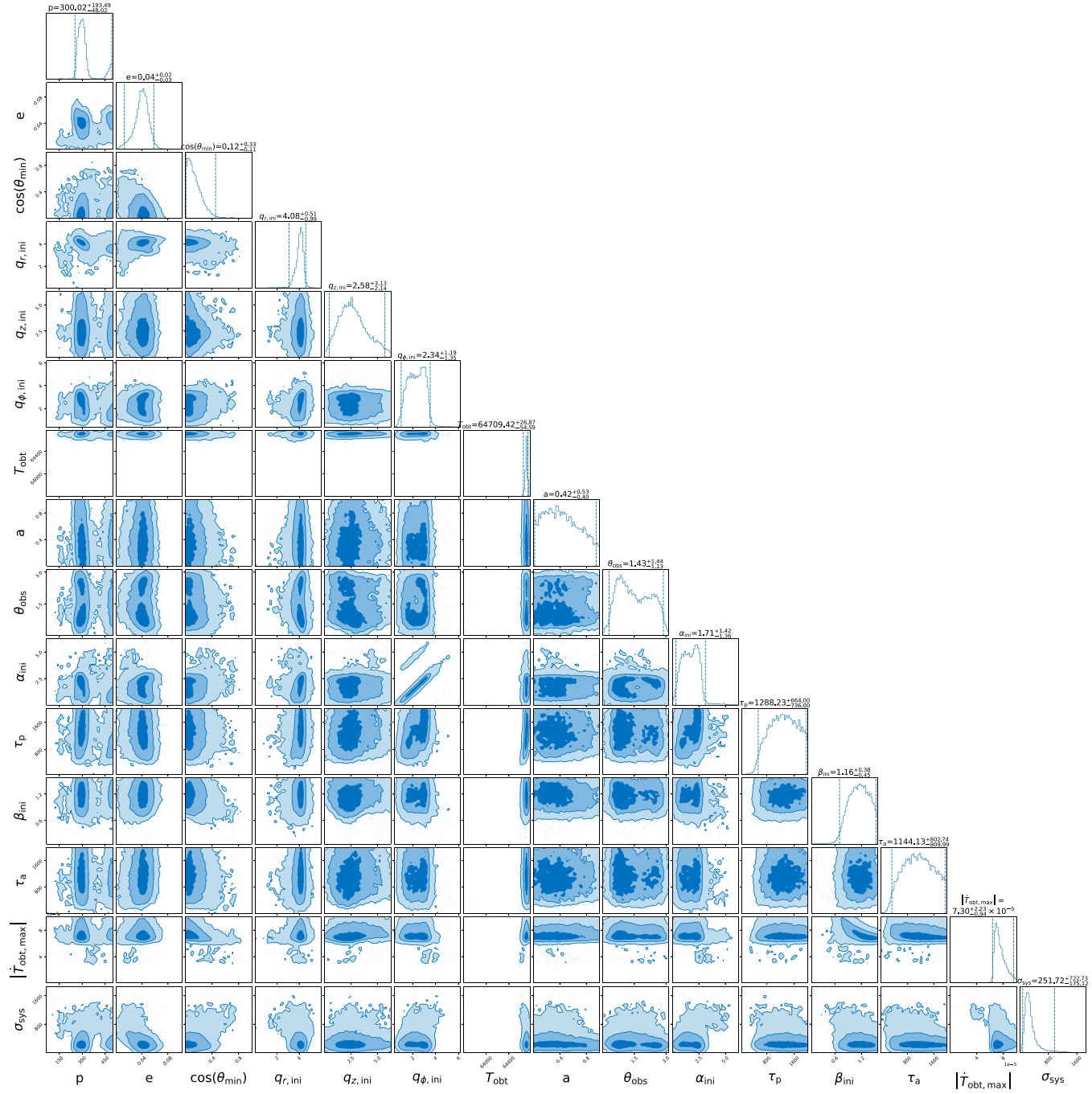

Figure A2. The posterior corner plot of model parameters for GSN 069 with the disc precession and alignment hypothesis ($\mathcal{H}_1$): $p[M_\bullet]$, e, $\cos\theta_{\rm min}$, $q_{r,\rm ini}$, $q_{z,\rm ini}$, $q_{\phi,\rm ini}$, $T_{\rm obt}$[s], a, $\theta_{\rm obs}$, $\alpha_{\rm ini}$, $\tau_{\rm p}$[d], $\beta_{\rm ini}$, $\tau_{\rm a}$[d], $\dot{T}_{\rm obt,max}[\times 10^{-5}]$, $\sigma_{\rm sys}$[s], where each pair of vertical lines denotes the 2σ confidence level.

APPENDIX B: O−C ANALYSIS OF GSN 069

For comparing with the Bayes analysis in the framework of EMRI + disc model, we apply a similar O−C analysis as in Miniutti et al. (2025) to GSN 069 data. In the top two panels of Fig. B1, we show the fitting result of a simple linear model, i.e. a constant period $T_{\rm trial}$,

$$\mathrm{O-C} = t^{(k)}_{\rm obs} - N_{\rm cyc} T_{\rm trial}\ , \tag{B1}$$

where $N_{\rm cyc}$ is the number of cycles and $T_{\rm trial} = 17.88$ h (Miniutti et al. 2025). In the O−C analysis, there is some ambiguity in identifying $N_{\rm cyc}$ of each flare due to data gaps, while it is of no such difficulty in the Bayes analysis of the EMRI + disc model. Therefore, we use the numbers $N_{\rm cyc}$ from the best-fit-ting EMRI + disc model in the O−C analysis. Note that the first flare in the last epoch is identified as the 213th flare, while it was identified as the 211th in Miniutti et al. (2025). From top panels of Fig. B1, the linear model of a constant period is insufficient to fit the data. In middle panels, we use a quadratic model

$$\mathrm{O-C_{quadratic}} = t^{(k)}_{\rm obs} - \left(T_{\rm obt} N_{\rm cyc} + \frac{1}{2}\dot{T}_{\rm obt}\langle T_{\rm obt}\rangle N^2_{\rm cyc}\right)\ , \tag{B2}$$

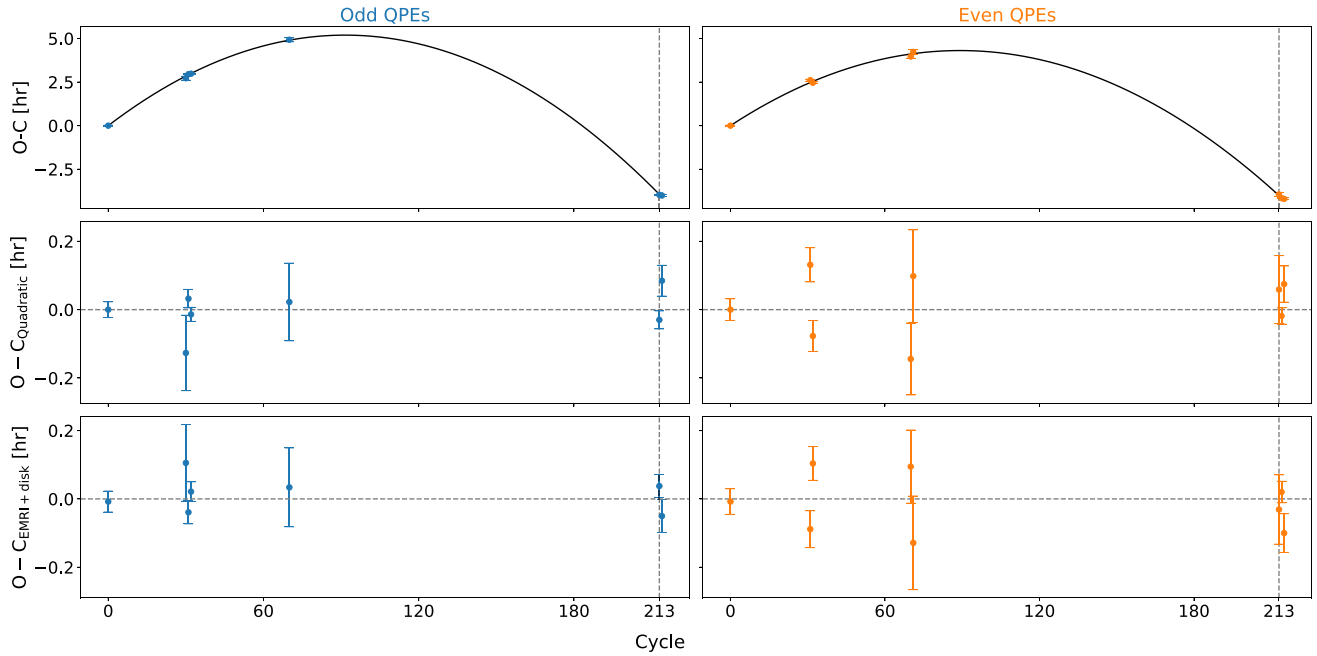

Figure B1. O−C analysis versus EMRI + disc model fitting to GSN 069 data, where error bars represent 1σ uncertainties. The number of cycles of the first flare in the last epoch is labelled by the dashed vertical line.

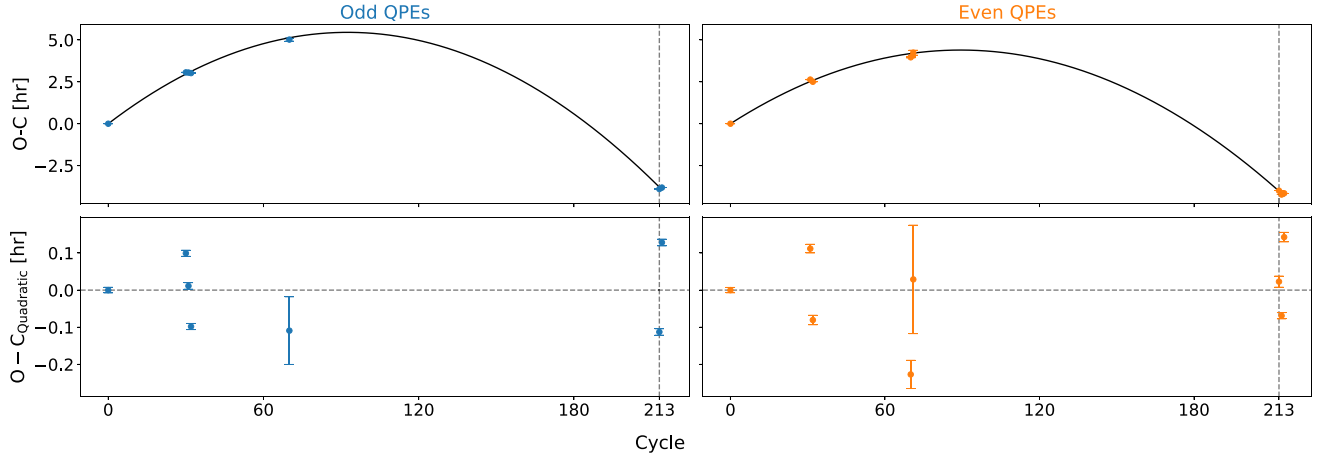

Figure B2. Same to Fig. B1 except for that flare peak times instead of flare starting times are used.

where $\langle T_{\rm obt}\rangle$ is the averaged orbital period across the whole time span assuming constant $\dot{T}_{\rm obt}$. Fitting the quadratic model to either the odd and even flares, orbital period and its derivative are constrained as

$$T_{\rm obt} = 64776^{+4}_{-4}\ {\rm s}\ ,$$
$$\dot{T}_{\rm obt} = -6.9^{+0.1}_{-0.1}\times 10^{-5}\ , \quad \text{(Odd flares)} \tag{B3}$$

and

$$T_{\rm obt} = 64715^{+8}_{-8}\ {\rm s}\ ,$$
$$\dot{T}_{\rm obt} = -6.1^{+0.1}_{-0.1}\times 10^{-5}\ , \quad \text{(Even flares)} \tag{B4}$$

at 2σ confidence level. The O−$C_{\rm quadratic}$ analysis does not yield clear in-phase or antiphase pattern in the residuals of even and odd flares. In the bottom panels are the residuals of the best-fitting QPE timing model with $\mathcal{H}_0$ for GSN 069, i.e. $t^{(k)}_{\rm obs} - t^{(k)}_0$, in which there is no clear signature of unmodelled superorbital modulation either.

Another possible source of discrepancy is the different ways of defining the QPE timing: we define a starting time for each flare and interpret it as when the star crosses the disc, while Miniutti et al. (2025) use the flare peak time. We again apply the O−C analysis to flare peak times and the results are displayed in Fig. B2. The results are quit similar to what is show in Fig. B1 except lower uncertainties of the flare peak times.

To summarize, there is some intrinsic ambiguity for identifying number of cycles of each flare in O−C analysis. This may lead to different interpretations of O−C analysis results and is likely the source of discrepancy between this work and Miniutti et al. (2025).

APPENDIX C: BEST-FITTING EMRI TRAJECTORIES DISC MOTION

In this section, we present the best-fitting EMRI trajectories with both $\mathcal{H}_0$ and $\mathcal{H}_1$ for the simulations in Section 4.3.

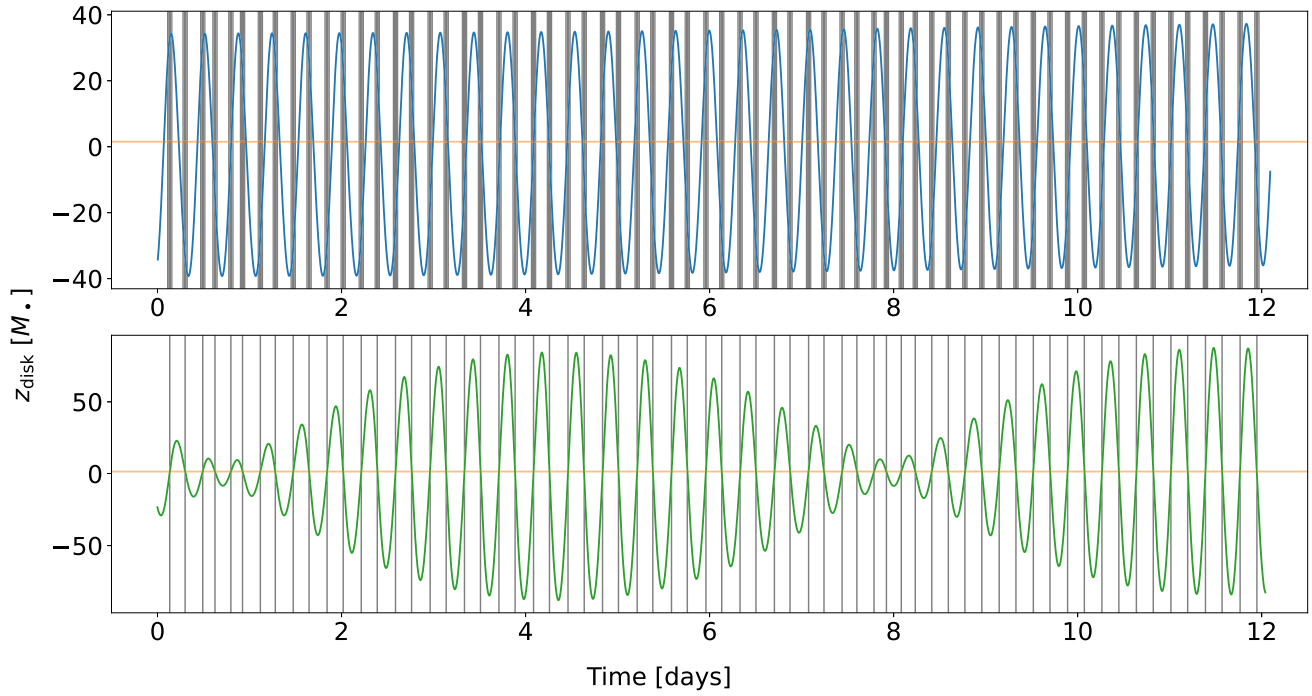

Figure C1. Best-fitting EMRI trajectories obtained with the two hypothesis in the fastest disc precession case with $\tau_{\rm p} = 7$ d, where $z_{\rm disc}(t)$ is the distance to the disc mid-plane. The vertical bands indicate the simulated data with inference uncertainties $t_0^{(k)} \pm \tilde{\sigma}(t_0^{(k)})$, where $\tilde{\sigma}(t_0^{(k)}) = \sqrt{(\sigma(t_0^{(k)}))^2 + \sigma_{\rm sys}^2}$. The orange horizontal line marks the disc surface. Upper panel: vanilla hypothesis ($\mathcal{H}_0$). Lower panel: disc precession and alignment hypothesis ($\mathcal{H}_1$). It is clear that $\mathcal{H}_1$ is much more favoured by the mock data.

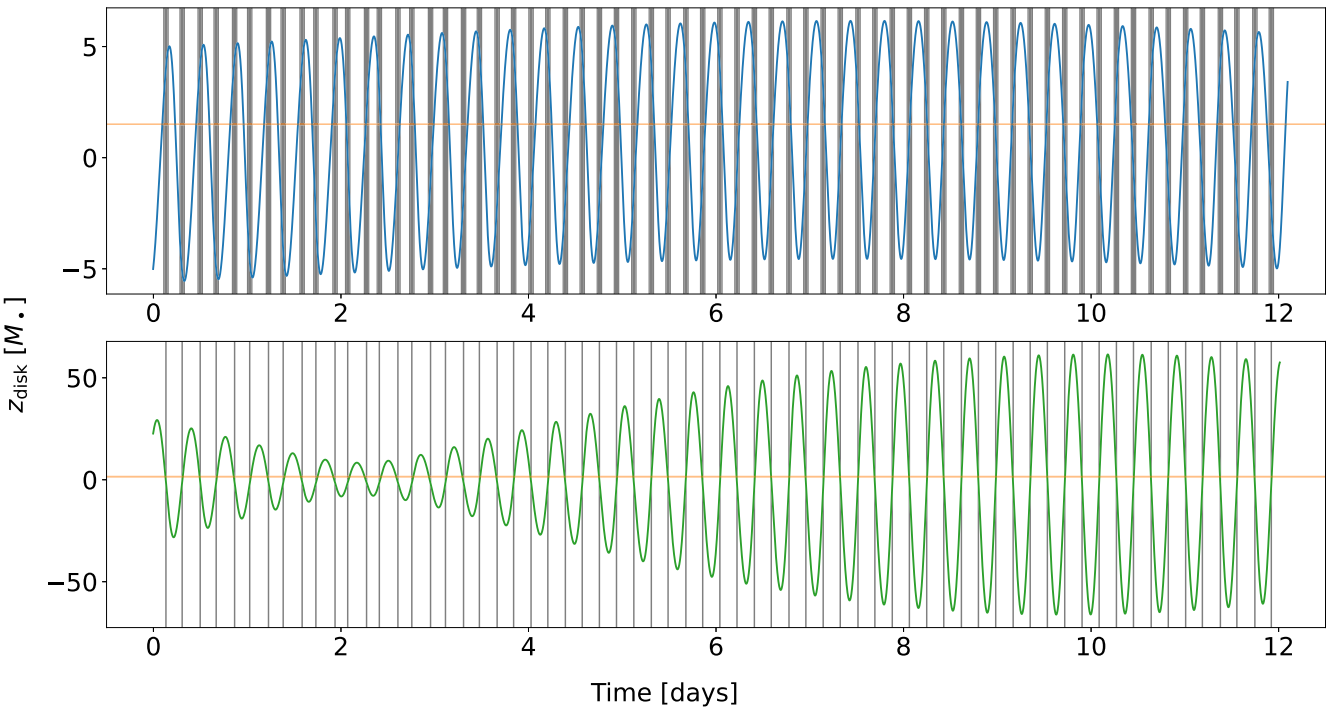

Figure C2. Same to Fig. C1 except for a precessing disc with $\tau_{\rm p} = 20$ d.

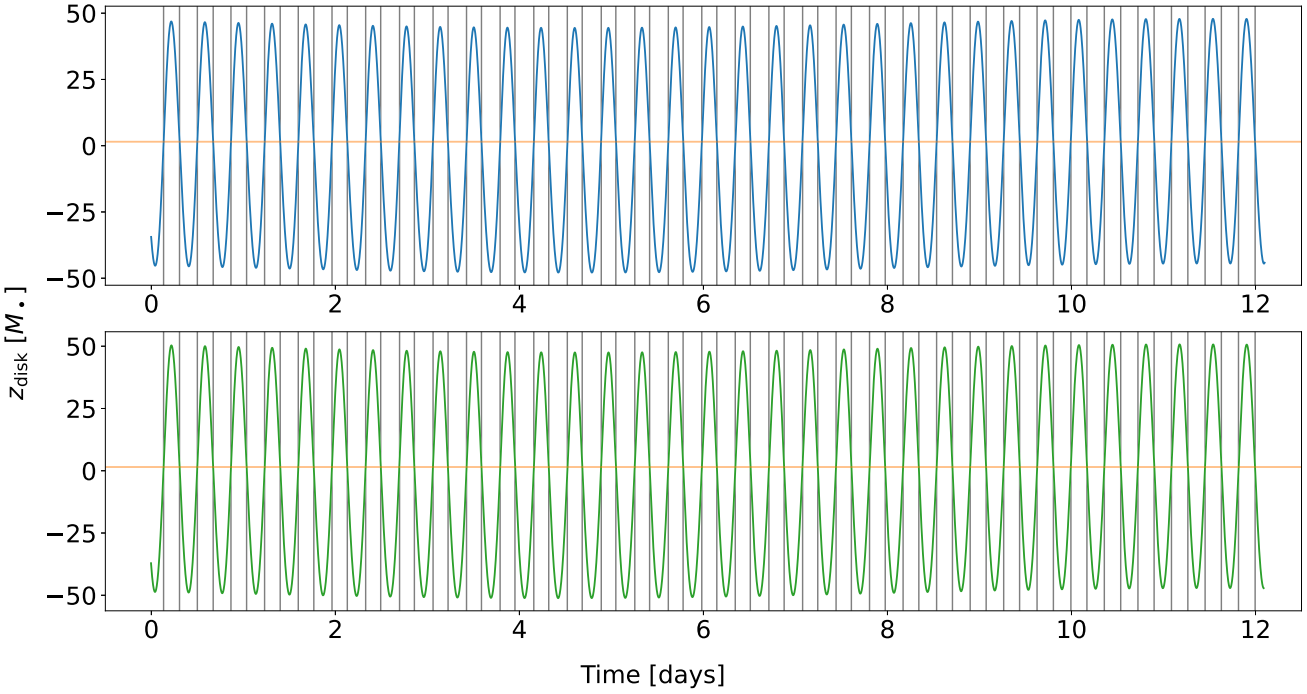

Figure C3. Same to Fig. C1 except for a slow precessing disc $\tau_{\rm p} = 150$ d.

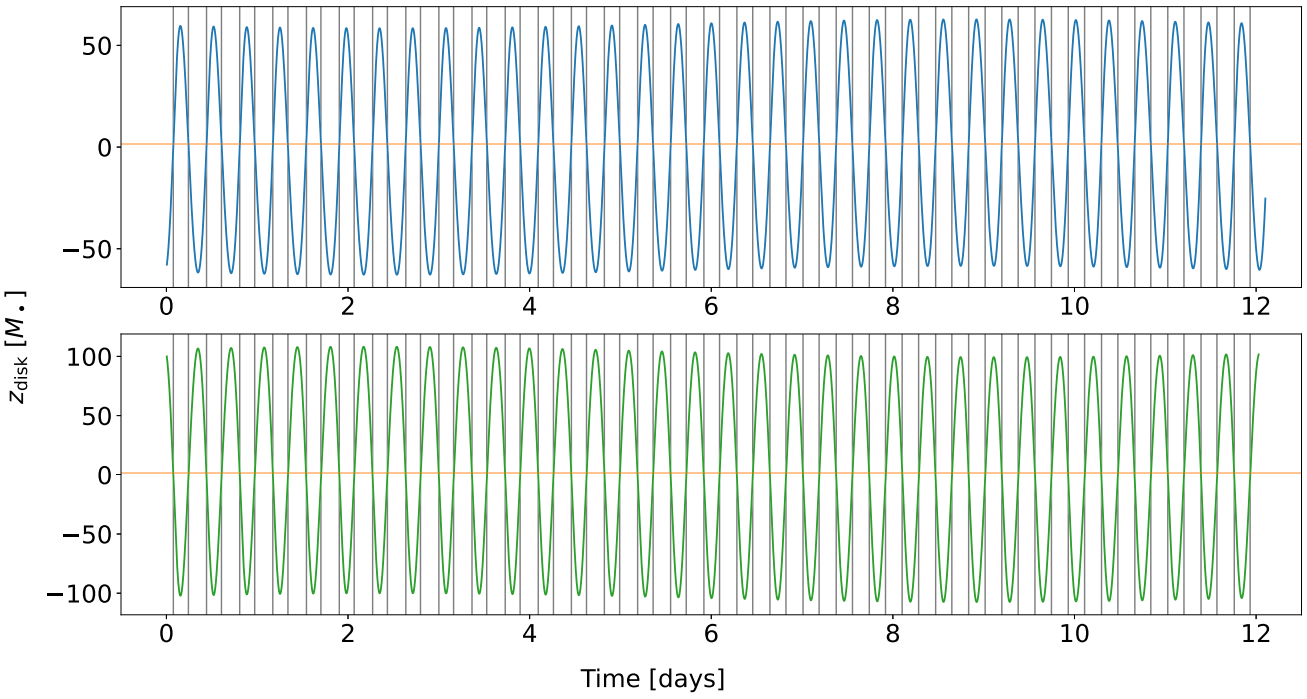

Figure C4. Same to Fig. C1 except for an equatorial disc $\tau_{\rm p} = \infty$ d. The upper panel is in fact the same as the upper panel in Fig. 4.

This paper has been typeset from a TEX/LATEX file prepared by the author.